Interplay between magnetism and band topology in Kagome magnets $R\mathrm{Mn_6Sn_6}$

Y. Lee,[1] R. Skomski,[2] X. Wang,[3] P. P. Orth,[1,4] A. K. Pathak,[5]
B. N. Harmon,[1,4] R. J. McQueeney,[1,4] I. I. Mazin,[6,7] and Liqin Ke[1]

[1] *Ames Laboratory, U.S. Department of Energy, Ames, Iowa 50011*
[2] *Department of Physics and Astronomy, Nebraska Center for Materials and Nanoscience, University of Nebraska, Lincoln, Nebraska 68588*
[3] *Sophyics Technology, LLC*
[4] *Department of Physics and Astronomy, Iowa State University, Ames, IA, 50011*
[5] *Department of Physics, SUNY Buffalo State, Buffalo, New York 14222*
[6] *Department of Physics and Astronomy, George Mason University, Fairfax, VA 22030*
[7] *Quantum Science and Engineering Center, George Mason University, Fairfax, VA 22030*

(Dated: April 5, 2022)

Kagome-lattice magnets $R\mathrm{Mn_6Sn_6}$ recently emerged as a new platform to exploit the interplay between magnetism and topological electronic states. Some of the most exciting features of this family are the dramatic dependence of the easy magnetization direction on the rare-earth specie, despite other magnetic and electronic properties being essentially unchanged, and the Kagome geometry of the Mn planes that in principle can generate flat bands and Dirac points; gapping of the Dirac points by spin-orbit coupling has been suggested recently to be responsible for the observed anomalous Hall response in the member $\mathrm{TbMn_6Sn_6}$. In this paper, we address both issues with density functional calculations and are able to explain, with full quantitative agreement, the evolution of magnetic anisotropy, including a complete reversal upon adding an f-electron with zero magnetic orbital quantum number when going from Ho to Er. We also show the microscopic origin of this computational result using a simple and physically transparent analytical model. We analyze in detail the topological properties of Mn-dominated bands and demonstrate how they emerge from the multiorbital planar Kagome model. We further show that, despite this fact, most of the topological features at the Brillouin zone corner K are strongly 3D, and therefore cannot explain the observed quasi-2D AHE, while those few that show a quasi-2D dispersion are too far removed from the Fermi level. We conclude that, contrary to previous claims, Kagome-derived topological band features bear little relevance to transport in $R\mathrm{Mn_6Sn_6}$, albeit they may possibly be brought to focus by electron or hole doping.

I. INTRODUCTION

Two-dimensional (2D) Kagome-lattices of $3d$ ions have initially attracted considerable attention due to their exceptionally strong magnetic frustration. The first experimental realizations were in systems featuring correlated Mott insulators based, for instance, on Cu^{2+}, with strong nearest neighbor antiferromagnetic exchange. These materials were investigated for potential spin liquid behavior [1] and fluctuation-driven phenomena such as unconventional superconductivity [2]. A relatively newer development is metallic Kagome materials with unusual magnetic and topological properties [3]. In particular, a 2D single-orbital Kagome model exhibits such features as flat band and Dirac crossing (DC). As we discuss later in the paper, the same features survive in the 2D five-orbital nearest-neighbor hopping Kagome planes, but not all of them retain their 2D character in real 3D materials like the family considered in this paper. Spin-polarized DCs may be gapped by the spin-orbit coupling (SOC) in quasi-2D ferromagnetic (FM) metals, resulting in Chern gaps [4–6]. When these topological electronic states are near the Fermi level, large Berry curvatures are manifested, resulting in novel quantum properties such as the quantum anomalous Hall effect.

An especially popular lately family of FM Kagome metals is $R\mathrm{Mn_6Sn_6}$, with the rare earth R=Gd, Tb, Dy, Ho, or Er (the structure also forms with non-magnetic rare earths but in that case the lack of the transferred FM interaction between the Mn layers bridged by a magnetic rare-earth leads to complex antiferromagnetic spiral structures). Intriguingly, and importantly, all of them form collinear ferrimagnets, but the direction of the ordered moments varies, seemingly randomly, from material to material. Given that SOC, as well as such properties as an Anomalous Hall Effect (AHE) or Magnetooptical Kerr Effect (MOKE), are intimately related to the direction of magnetization, understanding this interesting variation of the magnetic anisotropy is of utmost importance.

Another hot topic, prominently featured in the recent literature [13], is the possibility of Chern topological magnetism. In principle, Chern physics can be triggered by the DCs genetically related to the Kagome geometry. In that case, the size of the Chern gap is determined by the orbital characters of corresponding bands, as well as the size of the spin projection along the direction normal to the Kagome layer [4]. The prerequisites are (i) out-of-plane spin alignment, which is necessary for generating the Chern gap; (ii) minimal k_z dispersion of the relevant DCs; and (iii) proximity of the DC in question to the Fermi level.

The first condition is satisfied in, and only in, the Tb compound in the $R\mathrm{Mn_6Sn_6}$ family. This has motivated

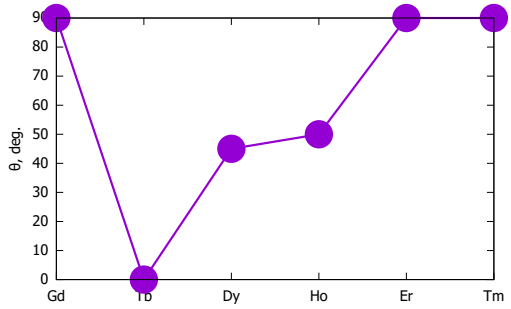

FIG. 1. Easy axis angle with respect to the crystallographic c direction in RMn$_6$Sn$_6$ at low temperature, with R = Gd, Tb, Dy, Ho, Er, and Tm [7–12].

intense research of this compound [13–18]. The main challenge here is establishing a connection between surface probes such as tunneling and bulk properties controlling effects like AHE and MOKE. Recently, Yin and coworkers, using tunneling spectroscopy, identified a feature that could be interpreted in terms of a DC located $\sim$ 130 meV above the Fermi level, and conjectured that this DC is a source of the observed bulk AHE. The intriguing observation depends on these quasi-2D DCs lying close to the Fermi level, and warrants a closer inspection, which is done in a companion paper [18].

In this work, we investigate the electronic structures and intrinsic magnetic properties of RMn$_6$Sn$_6$ with R = Gd, Tb, Dy, Ho, and Er. We demonstrate that the magnetization, exchange coupling, and magnetocrystalline anisotropy can be well described using *ab initio* methods, and understood within a simple analytical model based upon the crystal field (CF) at the rare-earth site, also calculated from first principles. We then address the topological aspect of the electronic structure, paying particular attention to the DCs, their location and origin, and their potential impact upon the bulk topological properties, and how they can be affected by spin-reorientation, surface effects, and electron correlation.

II. MAGNETIC ORDERING AND EXCHANGE COUPLING

RMn$_6$Sn$_6$ with heavy R elements crystallizes in the hexagonal HfFe$_6$Ge$_6$-type ($P6/mmm$, space group no. 191) structure, as shown in Fig. 2. R atoms (D_{6h}, or $6/mmm$) forms a triangular lattice with each R atom neighboring with six Sn$_2$ atoms in the basal plane. The nearest neighbor of R atoms is the Sn$_1$ atoms, which are along the axial direction and pushed slightly off the Mn Kagome plane by R atoms. The six Mn atoms ($2mm$) in the unit cell form two FM Kagome layers that sandwich the Sn$_3$ honeycomb layer and are FM coupled via the Mn-Sn$_3$-Mn superexchange [16]. Mn sublattices prefer easy-plane spin orientation. The couplings between neighboring Mn-bilayers blocks across the R-Sn$_1$ layer

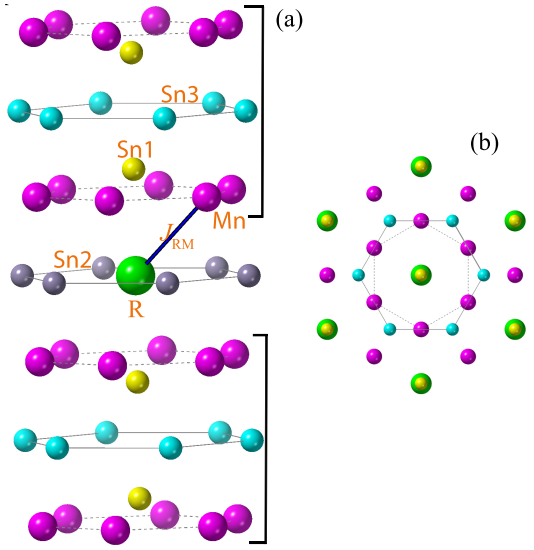

FIG. 2. Crystal structure of RMn$_6$Sn$_6$ (a) and its top view (b). Atomic layers are stacked in the order of [Mn-Sn$_1$-Sn$_3$-Sn$_1$-Mn]-[R-Sn$_2$]-[Mn-Sn$_1$-Sn$_3$-Sn$_1$-Mn] along the c axis. The Kagome Mn bilayers that sandwich the Sn$_3$ layer, denoted by the square brackets, are ferromagnetically strongly coupled, while the coupling between two Mn-bilayer blocks is weak. The antiferromagnetic coupling between the heavy rare-earth atoms R and neighboring Mn atoms, J_{RM}, is crucial to maintain the ferromagnetic Mn ordering in RMn$_6$Sn$_6$ at low temperature.

are weaker or even antiferromagnetic (AFM), depending on the R element type. As a result, the AFM R-Mn exchange coupling J_{RM} and R magnetic anisotropy are essential to determine the overall magnetic structure and band topology.

A. Spin and orbital magnetic moments

Table I summarizes the magnetic moments and their components in RMn$_6$Sn$_6$ calculated in DFT+U and compared with experimental values and the corresponding values expected for $4f$ shells from Hund's rules. Reported experimental spin-reorientation temperatures $T_{\rm SR}$ and Curie temperatures $T_{\rm C}$ are also listed for comparison. The experimental collinear magnetic structure and corresponding easy directions are adopted in the calculations.

The R-5d states are primarily spin-polarized by the neighboring 12 magnetic Mn atoms through the 3d-5d hybridization and further enhanced by the on-site $4f$ moment. The Mn spin aligns antiferromagnetically with the R-5d spin, which is parallel with the R-4f spin, resulting in R-Mn ferrimagnetic (FI) ordering in RMn$_6$Sn$_6$. Without considering the lattice parameters variation with R, the induced 5d spin moment can be written approximately as

$$m_{5d}^{(R)} = 12\alpha\, m_{3d}^{(\rm Mn)} + \beta\, m_{4f}^{(R)}, \qquad (1)$$

TABLE I. The spin magnetic moment m_R^s and orbital magnetic moment m_R^l of R atom (in μ_B/R), the total magnetic moments of Mn atom m_{Mn} (in μ_B/Mn), and magnetization M (in μ_B/cell) in RMn$_6$Sn$_6$ and compared to experiments. R-4f orbitals are treated within DFT+U. The calculated m_{Mn}, consisting of $\sim 1\%$ orbital magnetic moment, is antiparallel with R moment. Sn atoms have a moment of ~ 0.11 μ_B/Sn, and the interstitial has a moment of ~ 0.5 μ_B/f.u.; both align AFM with respect to the Mn moments. Electron occupancy in the minority R-4f channel $n_f^\downarrow$, spin magnetic moment m_{4f}^s, orbital magnetic moment m_{4f}^l, and total magnetic moment m_{4f} of R-4f electrons, according to Hund's rules, are also shown. On-site spin and orbital magnetic moments are in units of μ_B/atom. Experimental spin-reorientation temperature T_{SR} (in K) and Curie temperature T_C (in K) values are also listed.

R	Z	Hund's Rules				Calculations					Experiments					
		$n_{4f}^\downarrow$	m_{4f}^s	m_{4f}^l	m_{4f}	m_R^s	m_R^l	m_R	m_{Mn}	M	m_R	m_{Mn}	M	T_{SR}	T_C	References
Gd	64	0	7	0	7	7.33	-0.02	7.31	2.38	5.83	6.5	2.5	8.5		435–445	[8, 20, and 21]
Tb	65	1	6	3	9	6.26	2.96	9.23	2.42	4.10	9.2	2.39	5.77	310–330	423–450	[8, 17, 20, and 21]
Dy	66	2	5	5	10	5.21	4.96	10.18	2.40	3.05	9.97	2.11	2.69	270–320	393–410	[8, 20, and 21]
Ho	67	3	4	6	10	4.17	5.97	10.14	2.39	3.07	8.43	2.39	3.26–5.91	175–200	376–400	[8 and 21]
Er	68	4	3	6	9	3.19	5.93	9.12	2.38	4.03	8.40	2.21	4.86	75	340–352	[8, 20, and 22]

with $\alpha \approx 0.007$ and $\beta \approx 0.02$. The 5d spin moment decreases with the 4f spin moment and by $\sim 40\%$ when R goes from Gd to Er.

The calculated magnetic moments, as summarized in Table I, show good overall agreement with previously the reported experimental values. Mn moments are calculated to have values of 2.38–2.42 μ_B/Mn, consistent with the reported experimental values of 2.11–2.5 μ_B/Mn in various RMn$_6$Sn$_6$ compounds. For the magnetic moment of R atoms, experimental values also vary. The calculated value of $m_{Tb} = 9.23$ μ_B/Tb is nearly identical to the very recent experimental value measured by Mielke and co-workers [17] at 2 K. The calculated m_{Dy} also agrees well with neutron diffraction measurements [7, 17, 19]. For other R elements, the calculated m_R values are generally larger than reported experimental ones. Ho in HoMn$_6$Sn$_6$ has the largest difference between the calculated and experimental values, 10.14 and 8.43 μ_B/Ho, respectively. However, Clatterbuck *et al.* [20] estimated the net magnetic moment of HoMn$_6$Sn$_6$ from the magnetization curve at 10 K and obtained 3.26 μ_B/f.u., agreeing fairly well with the calculated value of 3.0 μ_B/f.u. Furthermore, larger experimental Ho moment measured by the neutron diffraction had been reported in doped HoMn$_6$Sn$_6$ compounds [12], e.g., with $m_{Ho} = 9.53\,\mu_B$ in HoMn$_6$Sn$_5$In. The difference between the experiments and theory may be relevant to the easy-cone orientation and the fact that we also partition magnetization into interstitial and Sn sites, which are AFM aligned with Mn.

B. Intersublattice R-Mn exchange coupling

The inter-sublattice magnetic couplings between R and Mn sublattice play an essential role in aligning the FM Mn-bilayers and stabilizing long-range Mn ordering. It also affects T_{SR} as a larger J_{RM} suppresses the thermal activation of 4f electrons into excited multiplet, which ultimately makes the thermal average of the 4f charge cloud more spherical and isotropic. We estimate the R-Mn coupling J_{RM} by mapping the total energies of FM and FI R-Mn spin configurations into a Heisenberg model defined as

$$H_{RM} = \sum_{i\in R, j\in Mn} J_{RM} S_i \cdot S_j \qquad (2)$$

Here, $S_i = m_i^s/2$ and m_i^s is the spin magnetic moment on site i. A positive J_{RM} corresponds to the AFM R-Mn coupling.

Figure 3 shows the R-Mn magnetic energy ΔE and exchange parameter J_{RM}, normalized with respect to the values of GdMn$_6$Sn$_6$, as functions of the electron occupancy in the minority R-4f spin channel [23]. The magnetic interaction energy $\Delta E = E_{FM} - E_{AFM} = 2J_{RM}S_R S_{Mn}$ is calculated as the energy difference between the AFM and FM spin configurations of R and Mn sublattices. To separate the chemical and structural effects, we also perform the calculations for all RMn$_6$Sn$_6$ compounds using the lattice parameters of GdMn$_6$Sn$_6$. The R-Mn intersublattice couplings are AFM for all R elements, consistent with experiments. The corresponding magnetic energy ΔE and exchange parameter J_{RM} decrease by $\sim 70\%$ and $\sim 30\%$, respectively, when R goes from Gd to Er. The abnormality of J_{RM} at R =Tb is related to the structural change, considering that the calculations that use the Gd lattice parameters give a smooth curve, as shown in Figure 3.

Besides the decrease of R spin moment, the reduction of R-Mn exchange energy from Gd to Er is caused by the weakening of J_{RM}. A similar decrease of J_{RM} has also been observed in other rare-earth transition-metal alloys, especially pronounced in light rare-earth series [24–26]. However, the mechanism behind the decreasing J_{RM} is not apparent; one may assume that J_{RM} should remain the same considering the similarities of band structures

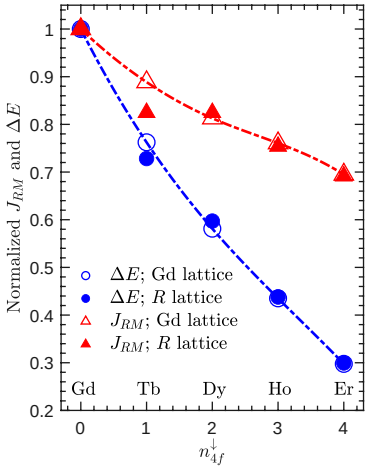

FIG. 3. Inter-sublattice R-Mn exchange coupling parameter J and magnetic energy ΔE as functions of the electron occupancy in R-4f minority spin channel $n^{\downarrow}_{4f}$ in RMn$_6$Sn$_6$ with R = Gd, Tb, Dy, Ho, and Er. $\Delta E = E_{\rm AFM} - E_{\rm FM}$ is calculated as the energy difference between the AFM and FM spin configurations of R and Mn sublattices. To separate the structural and chemical effects, calculations using the lattice parameters of GdMn$_6$Sn$_6$ are also carried out and denoted as open squares and circles.

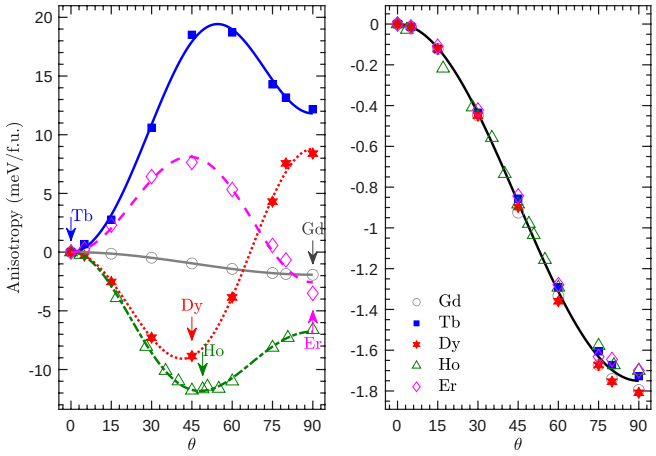

FIG. 4. Variation of magnetic energy (in meV/f.u.) as a function of spin-axis rotation in RMn$_6$Sn$_6$, with R = Gd, Tb, Dy, Ho, and Er, calculated (a) with and (b) without R-4f contributions. θ is the angle between the spin direction and the out-of-plane direction. The experimental easy directions for each compound are denoted by arrows in panel (a). The lines are just guides for the eye.

throughout the series. The exchange coupling between R-4f spin and Mn-3d spin is primarily through the R-5d electrons. The decrease of J_{RM} with increasing atomic number may be due to the lanthanide contraction, which reduces the overlap between 4f and 5d charge densities [27, 28]. The change of lattice parameters can also affect the 4f-5d overlap and 5d-3d hybridization, affecting the J_{RM}, as shown in the abnormality of J_{RM} at R =Tb in Fig. 3.

III. MAGNETOCRYSTALLINE ANISOTROPY

Magnetocrystalline anisotropy (MA) in RMn$_6$Sn$_6$ consists of contributions from both R and Mn sublattices. They have different temperature dependencies and dominate at lower temperatures and higher temperatures, respectively. MA becomes essential to maintain the long-range FM ordering in low-dimension materials or bulk materials consisting of magnetic layers that weakly coupled together, according to the Mermin-Wagner theorem [29, 30].

A. *Ab initio* calculations

At lower temperatures, experiments found that TbMn$_6$Sn$_6$ has an easy-axis anisotropy and ErMn$_6$Sn$_6$ has an easy-plane anisotropy, while the HoMn$_6$Sn$_6$ and DyMn$_6$Sn$_6$ have an easy-cone anisotropy with the quantization axis along the θ = 40–50° directions. Figure 4(a) shows the calculated total energies $E(\theta)$ as functions of spin-quantization direction, characterized by the angle θ deviated from the c axis. The calculated large easy-axis anisotropy in TbMn$_6$Sn$_6$ is comparable to the experimental value of 23.1 meV/f.u. measured recently using inelastic neutron scattering (INS) [16]. This value is also comparable to the well-studied SmCo$_5$ magnet [31]. The calculated easy directions for all five compounds agree well with experiments. GdMn$_6$Sn$_6$ shows a cosine-like $E(\theta)$ dependence, and the amplitude is one order of magnitude smaller than other RMn$_6$Sn$_6$ compounds. In contrast, all four other compounds show a non-monotonic dependence of E on θ with an energy minimum or maximum near 45°, suggesting substantial higher-order CF parameters (CFP) and MAE constants.

At higher temperatures, experiments [7, 8, 19] found that all compounds have an easy spin axis within the basal plane, suggesting the Mn sublattice has easy-plane anisotropy. Here, we theoretically confirm the easy-plane contribution of Mn sublattice by calculating the MAE contributions from non-4f electrons. This is achieved by treating R-4f electrons in the open-core approach, in which spherical R-4f charges do not contribute to MAE.

Figure 4(b) shows that Mn sublattices have easy-plane anisotropy as found in experiments. Unlike the total MAE, which contains the contribution from the R sublattice, the Mn MAE shows negligible higher-order terms as expected for non-4f elements. Moreover, remarkably, all compounds have a similar amplitude as calculated in GdMn$_6$Sn$_6$. Overall, MAE is generally weaker than the R-Mn exchange coupling in RMn$_6$Sn$_6$, which maintains a collinear spin configuration between R and Mn sublattices. As a result, at lower temperatures, the easy direction is dictated by the R sublattice. Furthermore, it is worth noting that although we often associate the

non-$4f$ MAE contribution with the Mn sublattice, in fact it is a combined effect of the Mn-$3d$ spin polarization and the large Sn-$4p$ SOC. This MA mechanism is rather general in many systems that consist of magnetic $3d$ atoms and heavier atoms, such as permanent magnet FePt [32], topologcial materials $MnBi_2Te_4$ [33], and magnetic 2D van der Waals matrials CrI_3 [34]. Ghimire *et al.* found that the MA in YMn_6Sn_6 consists of an easy-axis single-ion MA and a stronger easy-plane anisotropic exchange, resulting in an overall easy-plane MA [35].

The mechanism of the easy-cone axis in $DyMn_6Sn_6$ and $HoMn_6Sn_6$ is not well understood. For example, it has been argued that the easy-cone directions in $DyMn_6Sn_6$ and $HoMn_6Sn_6$ result from the competition between easy-plane Mn contribution and an easy-axis (weaker than those of Tb) contribution from the Dy or Ho sublattice [7, 19]. However, considering the Mn sublattice contribution is much smaller than the total MAE, we argue that Dy and Ho MAE themselves prefer the easy direction off the z-axis. To verify, we turn off the SOC on Mn and Sn sites in $HoMn_6Sn_6$ and find that the calculated easy direction remains the same. Thus, we conclude that the easy-cone axis results from the dominant Dy or Ho MAE itself instead of the competition between an easy-axis R MA and easy-plane Mn MA.

While the MA calculated in DFT agrees well with experiments for all RMn_6Sn_6 compounds we studied here, it is desirable to understand the evolution of rare-earth anisotropy further. In the following two sections, we elucidate the microscopic origin of this computational R anisotropy using simple and physically transparent analytical models.

B. Rare-earth anisotropy I: Phenomenological crystal-field model

The dominant rare-earth contribution to the magnetocrystalline anisotropy reflects the crystal-field interaction of the $4f$ electrons. This interaction was first described in terms of electrostatic interaction in insulators [36], but the theory also applies to covalent solids and metals, where it is often called ligand-field theory [37, 38]. Up to 4th order, the CF interaction of hexagonal crystals is described by the CFP A_2^0 and A_4^0 [36, 37, 39–41]. The anisotropy energy is, up to 4th order,

$$E_a = K_1 \sin^2(\theta) + K_2 \sin^4(\theta), \tag{3}$$

where

$$K_1 = -\frac{3}{2} A_2^0 Q_2 - 5 A_4^0 Q_4, \tag{4}$$

$$K_2 = \frac{35}{8} A_4^0 Q_4. \tag{5}$$

In these equations, the $Q_l = \Theta_l \langle r^l \rangle_{4f} \mathcal{O}_l^0$ are the electrostatic multipole moments of the rare-earth $4f$ shells; quadrupole moment $Q_2 = a_J \langle r^2 \rangle_{4f} \mathcal{O}_2^0$ and hexadecapole moment $Q_4 = b_J \langle r^4 \rangle_{4f} \mathcal{O}_4^0$. Here, the Stevens coefficients $a_J = \Theta_2$ and $b_J = \Theta_4$, the operator equivalents $\mathcal{O}_l^0$, and the rare-earth radii $\langle r^l \rangle_{4f}$ are well-known [39, 42], and low-temperature values of Q_2 and Q_4 have been tabulated in Ref. [40]. The distinguishing behavior of RMn_6Sn_6 is the large 4th-order CFP (A_4^0) and anisotropy (K_2) and the corresponding big energy minimum or maximum near 45°.

Element	$Q_2 \sim \theta_2$	$Q_4 \sim \theta_4$	Free Ions in a small field $+H_z$	Ions in an RMn6Sn6 Crystal Field
Tb	negative	positive	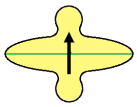	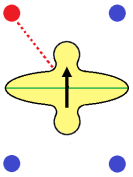
Dy, Ho	negative	negative	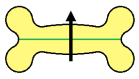	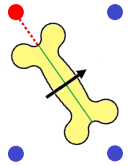
Er	positive	positive	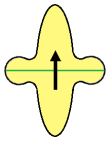	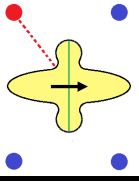

FIG. 5. Crystal-field origin of easy-axis (Tb), easy-cone (Dy, Ho), and easy-plane (Er) anisotropies in RMn_6Sn_6. The magnetization of free ions can point in any direction, so a small magnetic field $H = +H_z\hat{e}_z$ has been added to create a unique spin direction. In the crystal, symbolized by Mn ligands (blue, red), the spin direction is determined by the electrostatic interaction between the rare-earth $4f$ shell (yellow) and the Mn atoms. Crystal-field charges are negative, so the crystal-field (CF) interaction is repulsive. The right column focuses on the 4th-order interaction ($Q_4 \to K_2$), the dashed red line showing how the repulsive interaction with Mn stabilizes the spin structure. The green lines are the equators of the uniaxial $4f$ charge distribution, which is always perpendicular to the spin direction (arrows).

In isostructural compounds, A_2^0 and A_4^0 exhibit little change across the lanthanide series, because they reflect the crystalline environment of the rare-earth atoms. The fact that $TbMn_6Sn_6$ ($Q_2 < 0$ and $Q_4 > 0$) has the largest easy-axis anisotropy among the series suggests $A_2^0 > 0$ and $A_4^0 < 0$ (Indeed, we also confirmed $A_2^0 > 0$ and $A_4^0 < 0$ in DFT; see supplementary). The striking differences in Fig. 4(a) reflect the multipole moments. Physically, the strong SOC of the rare earths yields a rigid coupling between the spin and the orbital moments of the R atom, so that the magnetic anisotropy is determined by the electrostatic interaction of the R-$4f$ charge clouds

with the crystalline environment [40, 41]. The charge distribution of the Gd-$4f$ electrons is spherical (half-filled $4f$ shell), but the other lanthanides have aspherical charge distributions and exhibit nonzero anisotropy contributions. This asphericity provides a qualitative explanation of the curves in Fig. 4(a). Lowest-order interactions (Q_2) determine the basic spin orientation (easy axis vs. easy plane), but to understand easy-cone behavior, one needs Q_4 [41].

The R elements considered in this paper have $Q_4 > 0$ (Tb, Er) and $Q_4 < 0$ (Dy, Ho), as schematically shown in Fig. 5. Crystal-field charges in both metals and nonmetals are usually negative [38, 40], so that the Mn coordination of the R atoms in RMn$_6$Sn$_6$ (about 50°) yields a negative A_4^0 and realizes the situation outlined in Fig. 5. In a nutshell, for Dy and Ho, the combination of Q_2 and Q_4 creates a bone-like $4f$ charge distribution, and the electrostatic repulsion between the crystal-field charges (Mn) and the negatively charged $4f$ electrons causes the magnetization direction to deviate from the c-axis. This repulsion is exemplified, in Fig. 5, by dashed red lines near red-colored regions. In contrast, $Q_4 > 0$ in Tb and Er results in an energy maximum near $\theta \approx 45°$. Moreover, Tb and Er have similar 4th-order Stevens coefficients and their opposite Q_2 (oblate vs. prolate shape, respectively), produce easy-axis and easy-plane anisotropy, respectively. Note that $Q_l/\langle r^l\rangle$(Ho) $= -Q_l/\langle r^l\rangle$(Er), resulting in the roughly opposite $E(\theta)$ in ErMn$_6$Sn$_6$ and HoMn$_6$Sn$_6$. This can be understood considering that the total seven $4f$ electrons from Ho and Er will produce a nearly (or exactly, if we ignore element dependence of $\langle r^l\rangle$) spherical charge cloud with vanishing anisotropy.

Note that rare-earth anisotropy constants of order $n > 2$ are normally much smaller than second-order anisotropy constants [40], which explains the relatively rare overall occurrence of easy-cone magnetism. The high fourth-order anisotropy is a unique consequence of the Mn-coordination of the rare-earth atoms in the structure, which have 12 nearby Mn atoms in adjacent planes. CFP are proportional to the number of neighbors, each contributing an intrinsic crystal-field contribution A_n', and these intrinsic contributions are multiplied by coordination factors [38, 40]. For A_4^0, the coordination factor is $P_4(\cos\Theta) = (35\cos^4(\Theta) - 30\cos^2(\Theta) + 3)/8$, which has an extreme of -0.429 at 49.1° (see Fig. S5). Moreover, it is worth comparing RMn$_6$Sn$_6$ and the well-studied RCo$_5$ system. Despite the great structural similarity between RMn$_6$Sn$_6$ and the RCo$_5$ systems [31], A_2^0 is smaller in RMn$_6$Sn$_6$ compared to the latter, because there are Sn near neighbors both axially and in the plane, while in RCo$_5$, without the axial Sn and the dissimilarity between transition metal atom and Sn, the large 2nd-order anisotropy (K_1) dictate the anisotropy.

The above phenomenological crystal-field model provides an intuitive understanding of the easy directions in RMn$_6$Sn$_6$. To better quantify the CF model of the anisotropy, in the following we present a more quantitative analytical model of anisotropy using the CF energies from DFT.

C. Rare-earth anisotropy II: Analytical modeling using Crystal field levels

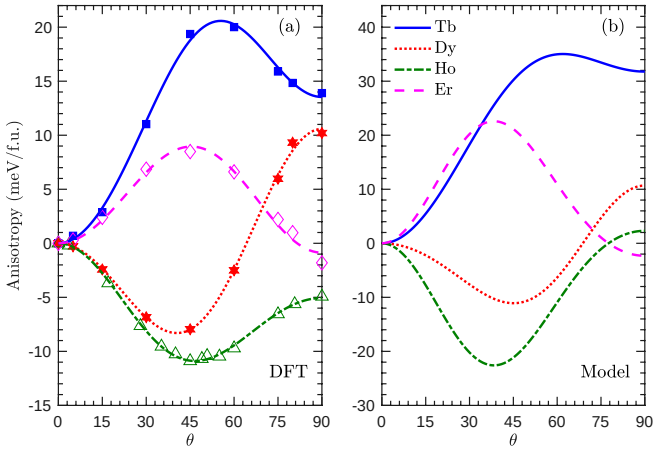

FIG. 6. R-$4f$ only single-ion anisotropy in RMn$_6$Sn$_6$ calculated in (a) DFT and (b) an analytic model Eq. (8)

In the case of SOC dominating the CF energy ($\xi \gg d$), one can assume that, in the first approximation, when the spin rotates, the angular moment follows it; for example, if the spin is rotated by θ, so is the angular moment, and the SOC energy remains the same during the rotation. Then, for instance, in the case of Tb, the wave function of its one f-electron is described by the *complex* spherical harmonic $\tilde{Y}_m^l = \tilde{Y}_3^3$ with the $\tilde{z}$ axis is rotated by θ from the crystallographic c axis. To calculate the CF energy of this rotated state, we need to re-expand this harmonic in terms of the original ones, namely, $\tilde{Y}_3^3 = \sum_m D_{3m}^3(\theta) Y_m^3$, where D are the reduced Wigner coefficients.

In the absence of SOC, CF splits the $4f$ states into five quenched levels characterized by *real* spherical harmonics $\mathcal{Y}_m^l$, which are linear combinations of $Y_{\pm m}^l$. Explicitly, $[\mathcal{Y}_m^l]^\intercal = \mathbf{U}[Y_m^l]^\intercal$, with $m = -3 \cdots 3$.

a_{2u}	e_{1u}	e_{2u}	b_{1u}	b_{2u}
z^3	$z^2(x \pm iy)$	$z(x \pm iy)^2$	$x(x^2 - 3y^2)$	$y(3x^2 - y^2)$
$\mathcal{Y}_0^3$	$\mathcal{Y}_{\pm1}^3$	$\mathcal{Y}_{\pm2}^3$	$\mathcal{Y}_{-3}^3$	$\mathcal{Y}_3^3$

Then the CF Hamiltonian becomes

$$\langle \tilde{Y}_m | H_{\rm CF} | \tilde{Y}_{m'} \rangle = (\mathbf{D}^\dagger \mathbf{U}^\dagger \mathbf{E} \mathbf{U} \mathbf{D})_{mm'} \qquad (6)$$

Here, $\mathbf{E}$ is the diagonal matrix of CF levels e_m, and $\mathbf{D} = \mathbf{D}(\theta)$ is the Wigner coefficient matrix corresponding to the Euler angles $(0, \theta, 0)$. Note that $e_0 = E(a_{2u})$, $e_{\pm1} = E(e_{1u})$, $e_{\pm2} = E(e_{2u})$, $e_{-3} = E(b_{1u})$ and $e_3 = E(b_{2u})$. The explicit expression of $E(\theta)$ from orbital m can be expanded in $\cos(i\theta)$ with $i = 0, 2, 4, 6$.

$$E_m(\theta) = \sum_{i=0,2,4,6} C_i^m \cos(i\theta). \quad (7)$$

For the second half of the lanthanide series with configurations $f^{n_\downarrow}$, we have

$$E(f^{n_\downarrow}, \theta) = \sum_{m=-3}^{n_\downarrow - 4} E_m(\theta) = \sum_{i=0,2,4,6} C_i^{n_\downarrow} \cos(i\theta). \quad (8)$$

Coefficients C_i^m and $C_i^{f^{n_\downarrow}}$ (with $i = 2, 4, 6$) are linear combinations of e_m (see details in Table S1).

We next extract CF levels e_m in $GdMn_6Sn_6$ within DFT+U and use them for all four R elements for simplicity, although CF splitting should decrease in heavier R compounds. Most importantly, the unphysical self-interaction contribution to CF in DFT is mostly avoided in $GdMn_6Sn_6$, thanks to a half-filled f shell. Using the calculated e_m, the modeled $E(\theta)$ are calculated and compared to DFT results in Fig. 6. The modeled MA somewhat overestimates the calculated MA, partly due to using the larger e_m of $GdMn_6Sn_6$. However, as crude as this approximation ($\xi \gg d$) is, it captures the key features of first-principles calculations quantitatively: (i) the scale of the quartic term is comparable with the scale of the quadratic term, (ii) the sextic term is negligible in Tb, but becomes increasingly more important toward Ho and Er, and (iii) the magnetic anisotropy energy as a function of the angle is approximately opposite in Er and Ho.

IV. BAND TOPOLOGY

One of the most enticing features of the Kagome lattice is the fact that, in the single-orbital nearest-neighbor tight-binding model, the electronic structures show a flat band and a DC at the K point in the Brillouin zone, where the latter is topologically protected while the former is not. In Chern-gapped insulators, edge states may significantly contribute to the transport properties by avoiding backscattering when E_F is located within the Chern gap.

$TbMn_6Sn_6$ is metallic. In the work of Yin *et al.* [13], the anomalous Hall effects were observed and related to possible 2D-like (weak k_z-dependent) SOC-gapped DC, mainly consisting of Mn inplane orbitals, slightly above E_F at the K point. On the other hand, Jones *et al.* [18] directly calculate the Berry curvatures and found that AHE actually comes from other parts of the BZ. To understand this discrepancy, we should analyze the nature and characters of multiple Dirac bands in the systems.

Here, we systematically investigate how the band structures near the Fermi level in RMn_6Sn_6 evolve with R, electron correlations, and spin reorientation. As we shown below, we found that the only quasi 2D DC is located about 0.7 eV above E_F, much higher than the value reported in the work of Yin *et al.* [13], which explains why Jones *et al.* [18] do not find significant contributions to AHE at the K point.

A. Dirac crossings and gap openings

It is instructive to expand single-orbital Kagome model Hamiltonian onto a more realistic five d-orbital model. In a hexagonal CF the d-orbitals split into three levels: $a_{1g} \propto \mathcal{Y}_0^2$, $e_g' \propto \{\mathcal{Y}_1^2, \mathcal{Y}_{-1}^2\}$, $e_g'' \propto \{\mathcal{Y}_2^2, \mathcal{Y}_{-2}^2\}$. They are orthogonal at the Γ point, but, of course, the corresponding bands can hybridize. Still, it is instructive to see what bands these states form on the Kagome lattice. Projected onto the ab plane, the a_{1g} state has s symmetry, i.e., the hopping is the same along all three bonds, characterized by vectors $\mathbf{a}_1$, $\mathbf{a}_2$, and $\mathbf{a}_3$. Considering only the nearest hopping, the Hamiltonian can be written as

$$\hat{H}_0 = t_0 \hat{\mathcal{H}} = t_0 \begin{pmatrix} 0 & \cos(\mathbf{k}\cdot\mathbf{a}_1) & \cos(\mathbf{k}\cdot\mathbf{a}_2) \\ \cos(\mathbf{k}\cdot\mathbf{a}_1) & 0 & \cos(\mathbf{k}\cdot\mathbf{a}_3) \\ \cos(\mathbf{k}\cdot\mathbf{a}_2) & \cos(\mathbf{k}\cdot\mathbf{a}_3) & 0 \end{pmatrix}, \quad (9)$$

which gives the famous band structure with one flat band and one DC at the K point.

The planar part of the e_g' states is simply $\exp(\pm i\varphi)$, so if there is hopping t_1 from the $|\mathcal{Y}_1^2\rangle$ state to the $|\mathcal{Y}_1^2\rangle$ state along a given bond, there will be $-t_1$ hopping between $|\mathcal{Y}_1^2\rangle$ and $|\mathcal{Y}_{-1}^2\rangle$. The Hamiltonian will be (the first three states are for the first orbital, the next three states for the second one):

$$\hat{H}_1 = t_1 \begin{pmatrix} \hat{\mathcal{H}} & -\hat{\mathcal{H}} \\ -\hat{\mathcal{H}} & \hat{\mathcal{H}} \end{pmatrix} \quad (10)$$

Diagonalizing this Hamiltonian gives the same bands as $\hat{H}_0$, plus three nonbonding flat bands at $E = 0$. For the e_g'' states it is $\exp(\pm 2i\varphi)$, so there is no sign flip, but the band structure is exactly the same. So, overall we expect to see 3 DCs per spin, per layer, so 3 k_z-dependent Dirac lines, each of them folding back from K to H, so 6 non-degenerate DCs at K and 3 degenerate (or just close in energy) at H. Of course, some of them may be shadowed by hybridization among themselves and with other bands. Only the e_g'' bands are expected to give more or less 2D bands, one for each spin. All DCs in the same spin channel are spread over the the energy range of the order of the Mn CF, that is, several eV.

Since only one out of the three DCs are two dimensional, it becomes extremely important to identify them in the calculated band structure. This can be achieved by plotting bands along the $K - H$ path, or plotting the band structures projected on the surface BZ, in which the dispersive (along k_z) band will be washed out and quasi 2D bands will be visible.

Near the Fermi energy, all five compounds share similar band structures, as the non-4f electrons dominate in this energy range. Multiple DCs occur at the K-point near E_F, below or above E_F, as expected from the discussion above for the multiorbital kagome Mn lattice.

SOC splits the crossings and opens gaps of various sizes at BZ corners if the spin is along the z direction. However, as expected, most of them strongly depend on k_z, reflecting the 3D nature of the corresponding bands. To better illustrate the k_z dependence of band structures, we project all bands onto the surface BZ by integrating the $\mathbf{k}$-dependent spectral function, over k_z,

$$I(\mathbf{k}_\parallel, \omega) = \int_0^1 \mathrm{d}k_z \sum_i \delta[\omega - E_i(\mathbf{k}_\parallel, k_z)]. \quad (11)$$

Here, k_z is integrated from 0 to 1 r.l.u., while $\mathbf{k}_\parallel$ is in the basal plane.

Figure 7(a) compares the projected $TbMn_6Sn_6$ bands along the 2D path Γ-K-M. calculated without and with SOC in DFT, shown as blue and red bands, respectively. Two occupied DCs occur at ~ 0.05 and ~ 0.2 eV below E_F, respectively, whose gaps are barely opened by SOC. The most prominent k_z-independent DC lies $\sim$0.7 eV above E_F, dominated by the Mn-3d characters (see Table S2). In contrast to the two occupied DCs, a much larger gap is induced at this DC when SOC is included, agreeing with the previous report [13]. Note that the position of this Dirac crossing is much higher than the previously reported value of $\sim$0.13 eV above E_F [13], and is unlikely to play a significant role in transport properties. The gap size depends on the band characters at these DCs and how effectively SOC can couple them. Other RMn$_6$Sn$_6$ compounds show overall similar band structures (see Fig. S3).

B. Effects of Mn-3d electron correlation

$TbMn_6Sn_6$ is, as mentioned, a good metal, and Mn electrons are on the itinerant side. Yet, these d electrons are still considerably, albeit not strongly localized, so correlation effects may be important. By analogy with such systems as Sr_2RuO_4 and Fe-based superconductors, one may expect a "Hund's metal" behavior. This is rather hard to capture in static methods such as LDA+U or hybrid functionals. Even the Dynamical Field Theory (DMFT), the most common method to account for fluctuational correlations, faces serious problems in materials like ours, where long-range correlations are expected and hybridization with Sn is crucial, and good DMFT calculations are likely unfeasible for such a 13-atom unit cell. Lacking this, the most we can hope is to assess the correlation effects using the simplest available technique, LDA+U, keeping in mind that this is likely a too simple approach to draw quantitative conclusions.

LDA+U technique comes in several flavors. They differ by the precise recipe to exclude the double counting of the of the local Coulomb interactions and by including the angular dependence of the Hund's J. The most widely used recipe is the one that gives the correct limit in case of fully localized electrons (FLL), and it is generally considered more physical[43]. However, it is known

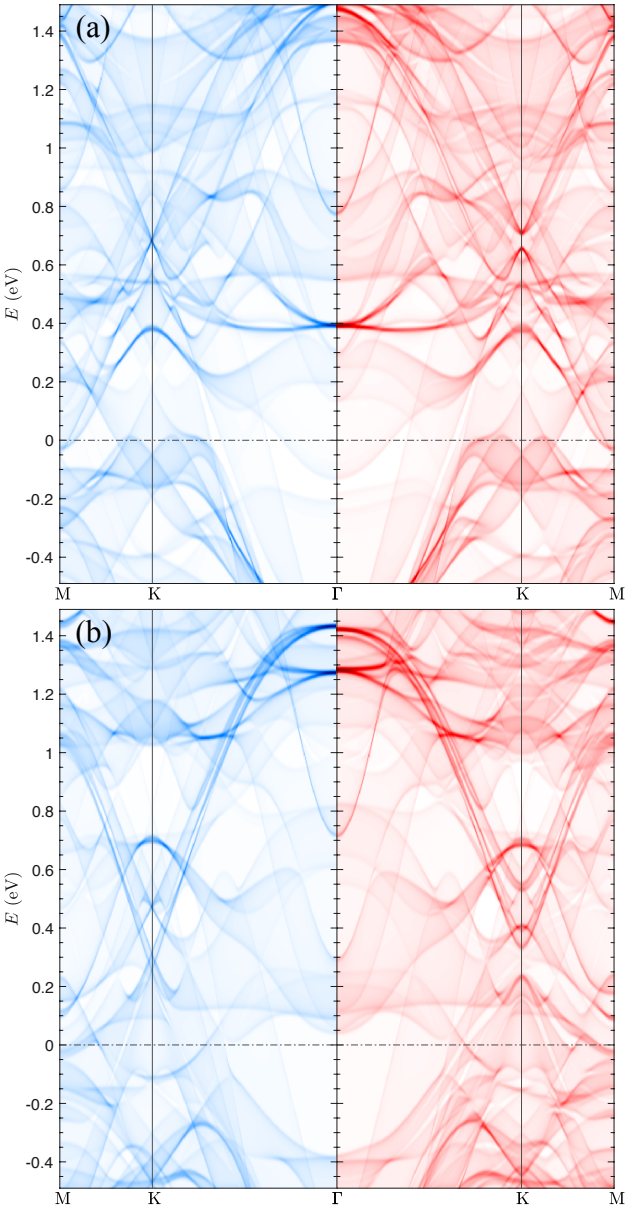

FIG. 7. Band structures projected on surface BZ calculated without (blue) and with (red) SOC in $TbMn_6Sn_6$. The k-dependent DOS are integrated along k_z (see Eq. (11)) and are calculated in (a) DFT and (b) DFT+U. Hubbard $U = 2.5$ eV and Hund's rule coupling $J = 0.7$ eV are applied on Mn-3d orbitals, and the AMF double-counting scheme is employed in DFT+U.

to systematically increase the equilibrium magnetic moments, which are already too large in $TbMn_6Sn_6$. This is correct physical behavior, because fluctuations, neglected in LDA+U, work in the opposite direction, reducing the averaged magnetic moment. On the other hand, and alternative recipe, called AMF (from "around mean field"), does not have this property; that is to say, FLL more correctly reproduces the *instantaneous* magnetic moment, while AMF gives a better estimate for the *average* magnetization. Since it is the latter that mostly affects the

electronic structure, we decided to try the AMF prescription.

Computational details are discussed in the Supplementary material. Here we show in Fig. 7(b) the bands obtained in LDA+U compared to the straight DFT bands. The main difference is that the quasi-2D DC at ~ 0.7 eV above E_F shifts down to ~ 0.3 eV (still too far to affect the transport properties though) and the SOC-induced gap at the same DC is increased by about a factor of two. As mentioned, we are not insisting on these exact numbers, but this result suggests that the correlation effects may modify the relevant aspects of the band structure. Ultimately better experiments will be needed to get the final answer.

C. Effects of spin orientation

It is well known that Kagome materials in the presence of SOC and out-of-plane magnetization effectively realize the Haldane model for a Chern insulator without Landau levels [4, 5, 13, 44]. This model describes spin-polarized electrons hopping in a background of staggered magnetic fluxes on a lattice that supports Dirac crossings in the absence of the magnetic field. In RMn$_6$Sn$_6$, the bands that are mostly localized in the Mn Kagome layer naturally exhibit DCs at the K and K' points near $E_{\rm F}$, as shown in Fig. 8. Due to FM order, these DCs occur within a single spin channel, which can be Chern gapped by intrinsic SOC (see Eq. (S2)). Besides the itinerant band character, e.g., the 3d-orbital characters of Mn atoms in the Kagome lattice, the size of the SOC-induced gaps also depends on the spin orientations of magnetic Mn atoms, which can evolve with the R element type and with temperature [45]. Temperature- and substitution-induced spin reorientations thus have direct consequences on topological transport properties such as the quantum anomalous Hall conductivity, if these (gapped) crossings occur close to the Fermi energy.

For example, the gap size should vary when RMn$_6$Sn$_6$ goes from the easy-axis TbMn$_6$Sn$_6$ to easy-cone HoMn$_6$Sn$_6$ or when RMn$_6$Sn$_6$ is heated above the spin-reorientation temperatures. Figures 8(a) and 8(b) show the band structures in HoMn$_6$Sn$_6$ calculated without and with SOC, respectively. For the simplicity of illustration, here we focus on the large gap of the DC at 0.7 eV, labeled as DC4 in Fig. 8(a). Figure 8(b) shows the gap almost vanishes when the spin-quantization axis rotates from the out-of-plane direction to the in-plane direction. This can be understood by starting from the non-SOC band structures and treating SOC within perturbation theory.

DC4 mainly consists of $\mathcal{Y}^2_{\pm 2}$ and $\mathcal{Y}^2_0$ Mn-3d characters (see Table S2) in the minority spin channel. Since the DCs occur within the same spin channel, the gap size Δ is proportional to the spin-parallel part of $H_{\rm so}$, as shown in Eq. (2), and can be written as

$$\Delta \propto L_z \cos(\theta) + f(L_+, L_-, \theta, \varphi). \qquad (12)$$

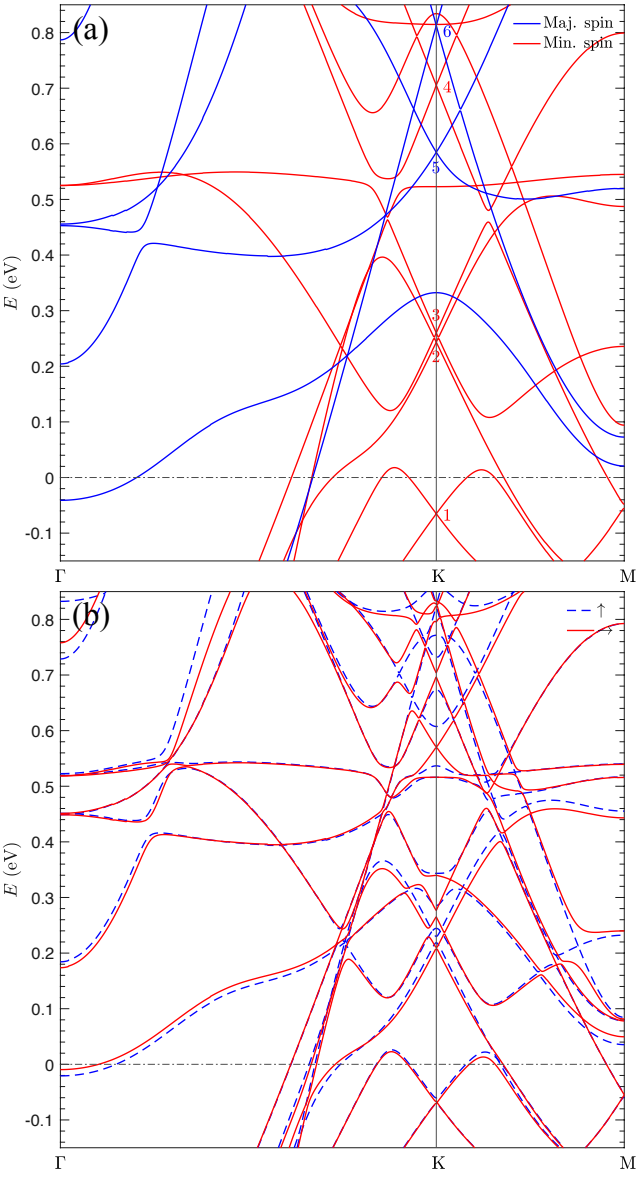

FIG. 8. Band structure near $E_{\rm F}$ in HoMn$_6$Sn$_6$ calculated (a) without SOC and (b) with SOC. In panel (a), the majority-spin and minority-spin, referred to Mn site, are in blue and red, respectively. In panel (b), the band structures are calculated with the spin-quantization axis along the out-of-plane (blue dashed line) and in-plane (red solid line) directions. Both magnetic sublattices are ordered. The gap sizes depend on spin orientations.

The second term in Eq. (12) vanishes because $L_\pm$ do not couple between $\mathcal{Y}^2_{\pm 2}$ and $\mathcal{Y}^2_0$ states [46]. Thus, the gap size is solely determined by $L_z \cos(\theta)$, which vanishes at $\theta = 90^\circ$ with the in-plane spin orientations. Thus, if the DCs near K are responsible for AHE observed, one may expect a significant change in the measurement near $T_{\rm SR}$.

The band characters of other DCs may consist of orbitals that can also be coupled by $L_\pm$. The corresponding SOC-induced gap can remain open when spin is in-plane. Moreover, DCs contains a larger Sn component can have

a larger gap, as Sn has a much larger SOC constant than Mn. Finally, when DCs are next to each other, multiple DCs can be coupled by SOC, complicating the analysis.

D. Surface effects on magnetism and bandstructure

Finally, we investigate the surface effects on the magnetism and electronic structures in RMn$_6$Sn$_6$. Experimentally, purely Mn Kagome lattices without detectable defects have been observed over a large field of view [13] in TbMn$_6$Sn$_6$. Here, we calculate the electronic structures in monolayer and bilayer TbMn$_6$Sn$_6$ with terminating Mn surface on one side and R-Sn surface on the other side. Each layer is one f.u. thick, as shown in Fig. 2, and contains two Mn Kagome planes. Sufficiently large vacuum space is used in the unit cell to avoid the interaction between neighboring slabs due to periodic boundary conditions. The structure is relaxed so that the force on each atom is less than 1 mRy/a.u.

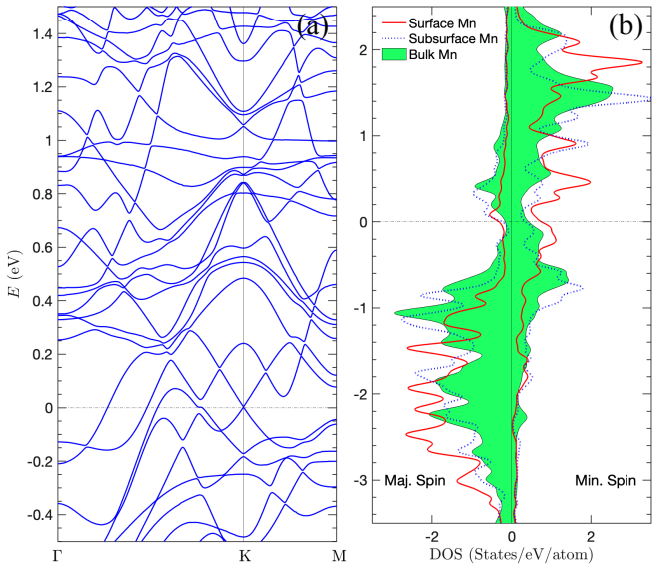

FIG. 9. (a) Band structures and (b) partial density of states projected on the surface (red solid line) and subsurface (blue dashed line) Mn sites in monolayer TbMn$_6$Sn$_6$. In panel (b), bulk Mn (green filled area) DOS is also shown to compare.

Both monolayer and bilayer TbMn$_6$Sn$_6$ remain metallic as in bulk. The Tb atom on the surface has a slightly larger magnetic spin moment than that of subsurface Tb in a bilayer TbMn$_6$Sn$_6$. In contrast, remarkably, the surface Mn atoms have much larger magnetic moments and stronger exchange splittings than in the bulk case. For both monolayer and bilayer cases, Mn atoms on the terminating surface have a magnetic moment of 3.3 μ_B/Mn, while the subsurface Mn layers have a similar moment of $\sim$2.4 μ_B/Mn as in the bulk case. As a result, near the Fermi level, the spin splitting of the surface Mn states increases. Figure 9 shows the band structures, and partial density of states projected on surface and subsurface Mn layers in monolayer TbMn$_6$Sn$_6$. The band structures change profoundly compared to the bulk band, and interestingly, a DC occurs at K at E_F. A larger spin splitting for the surface Mn states, induced by their larger moments, are shown in Fig. 9(b). Overall, RMn$_6$Sn$_6$ is quite different from 2D van der Waals materials, where the calculated on-site moment and intralayer magnetic couplings remain similar in bulk and monolayer forms [34].

V. CONCLUSIONS

In summary, we have systematically investigated the electronic structures and intrinsic magnetic properties of RMn$_6$Sn$_6$ for R = Gd, Tb, Dy, Ho, and Er. In particular, we revealed a non-monotonic dependence of the magnetic energy E on the magnetic quantization axis θ for all compounds except GdMn$_6$Sn$_6$, suggesting the importance of higher-order MAE parameters. Our calculations show that TbMn$_6$Sn$_6$ has an easy-axis, GdMn$_6$Sn$_6$ and ErMn$_6$Sn$_6$ have an easy-plane anisotropy, while DyMn$_6$Sn$_6$ and HoMn$_6$Sn$_6$ have easy-cone anisotropy with the easy axis deviating from the c axis by $\theta = 45°$ and 49°, respectively. All these results agree well with experimental observations. We further demonstrated that the easy-cone anisotropy in DyMn$_6$Sn$_6$ and HoMn$_6$Sn$_6$ results from the dominant R MA itself instead of the competition between an easy-axis R MA and the easy-plane Mn MA. Finally, we showed that the seemingly irregular variation of the easy direction with the rare earth cam be rather accurately described analytically without any adjustable parameters (the crystal field levels being calculated *ab initio*) and stems from mathematical properties of Wigner matrices.

We have further investigated the band structures in RMn$_6$Sn$_6$ and how Dirac crossings and SOC-induced gaps evolve with the type of R atom, additional electron correlations, and spin reorientation. The multitude of DCs can be qualitatively understood by solving the appropriate five-d-orbitals tight-binding model. In the DFT calculations, the most prominent SOC-gapped 2D-like DC is located at about 0.7 eV above E_F. Including additional electron correlation of Mn-3d orbitals beyond DFT, on a simplified level of AMF-LDA+U, however, affects the positions of DCs near E_F, and, for instance, moves the 2D crossing discussed above from $\sim$ 0.7 to $\sim$ 0.3 eV, and increases the amplitude of the SOC gap. One needs keep in mind though that it is notoriously difficult to include moderate-strength correlations in itinerant metals, and, for instance, the popular Dynamic Field Theory method misses nonlocal correlations, crucial in itinerant systems, and the results are critically sensitive to the number of orbitals included in consideration. Thus, our result should be taken with a grain of salt as mere indication that correlation effects may change the band picture in a meaningful way. Direct

experimental probes such as ARPES or quantum oscillation spectroscopy are thus highly desirable in the R166 family.

Finally, unlike 2D van der Waals materials, we observe that in $R\mathrm{Mn_6Sn_6}$ the Mn moments on the terminating Mn Kagome surface can have a much larger moment of $3.3\,\mu_\mathrm{B}$/Mn, and correspondingly an enhanced exchange splitting that affects the positions of Dirac crossings. Such predicted enhancement of the surface Mn moment remains to be confirmed experimentally.

ACKNOWLEDGMENTS

The authors gratefully acknowledge discussions with Q. Niu and N. Ghimire. LK and YL are supported by the U.S. Department of Energy, Office of Science, Office of Basic Energy Sciences, Materials Sciences and Engineering Division, and Early Career Research Program. RJM and PPO are supported by the U.S. Department of Energy, Office of Basic Energy Sciences, Division of Materials Sciences and Engineering. Ames Laboratory is operated for the U.S. Department of Energy by Iowa State University under Contract No. DE-AC02-07CH11358. The work in Nebraska is supported by the National Science Foundation/EPSCoR RII Track-1: Emergent Quantum Materials and Technologies (EQUATE), Award OIA-2044049. IM acknowledges support from DOE under the grant DE-SC0021089. This research used resources of the National Energy Research Scientific Computing Center (NERSC), a U.S. Department of Energy Office of Science User Facility operated under Contract No. DE-AC02-05CH11231.

[1] M. R. Norman, Colloquium: Herbertsmithite and the search for the quantum spin liquid, Rev. Mod. Phys. **88**, 041002 (2016).

[2] I. I. Mazin, H. O. Jeschke, F. Lechermann, H. Lee, M. Fink, R. Thomale, and R. Valentí, Theoretical prediction of a strongly correlated dirac metal, Nature Communications **5**, 4261 (2014).

[3] N. J. Ghimire and I. I. Mazin, Topology and correlations on the kagome lattice, Nature Materials **19**, 137 (2020).

[4] G. Xu, B. Lian, and S.-C. Zhang, Intrinsic Quantum Anomalous Hall Effect in the Kagome Lattice $\mathrm{Cs_2LiMn_3F_{12}}$, Phys. Rev. Lett. **115**, 186802 (2015).

[5] E. Tang, J.-W. Mei, and X.-G. Wen, High-Temperature Fractional Quantum Hall States, Phys. Rev. Lett. **106**, 236802 (2011).

[6] T. Neupert, L. Santos, C. Chamon, and C. Mudry, Fractional Quantum Hall States at Zero Magnetic Field, Phys. Rev. Lett. **106**, 236804 (2011).

[7] B. El Idrissi, G. Venturini, B. Malaman, and D. Fruchart, Magnetic structures of $\mathrm{TbMn_6Sn_6}$ and $\mathrm{HoMn_6Sn_6}$ compounds from neutron diffraction study, Journal of the Less Common Metals **175**, 143 (1991).

[8] G. Venturini, B. E. Idrissi, and B. Malaman, Magnetic properties of $R\mathrm{Mn_6Sn_6}$ (R = Sc, Y, Gd–Tm, Lu) compounds with $\mathrm{HfFe_6Ge_6}$-type structure, Journal of Magnetism and Magnetic Materials **94**, 35 (1991).

[9] M. Dirken, R. Thiel, J. Brabers, F. de Boer, and K. Buschow, ^{155}Gd Mössbauer effect and magnetic properties of $\mathrm{GdMn_6Sn_6}$, Journal of Alloys and Compounds **177**, L11 (1991).

[10] G. Venturini, R. Welter, B. Malaman, and E. Ressouche, Magnetic structure of $\mathrm{YMn_6Ge_6}$ and room temperature magnetic structure of $\mathrm{LuMn_6Sn_6}$ obtained from neutron diffraction study, Journal of Alloys and Compounds **200**, 51 (1993).

[11] G. Venturini, D. Fruchart, and B. Malaman, Incommensurate magnetic structures of $R\mathrm{Mn_6Sn_6}$ (R = Sc, Y, Lu) compounds from neutron diffraction study, Journal of Alloys and Compounds **236**, 102 (1996).

[12] C. Lefèvre, G. Venturini, and B. Malaman, Neutron diffraction study of the magnetocrystalline anisotropy in $\mathrm{TbMn_6Sn_{5.8}Ga_{0.2}}$, $\mathrm{TbMn_6Sn_5Ga}$, $\mathrm{HoMn_6Sn_5Ga}$ and $\mathrm{HoMn_6Sn_5In}$ compounds, Journal of Alloys and Compounds **358**, 29 (2003).

[13] J.-X. Yin, W. Ma, T. A. Cochran, X. Xu, S. S. Zhang, H.-J. Tien, N. Shumiya, G. Cheng, K. Jiang, B. Lian, *et al.*, Quantum-limit Chern topological magnetism in $\mathrm{TbMn_6Sn_6}$, Nature **583**, 533 (2020).

[14] X. Xu, J.-X. Yin, W. Ma, H.-R. Tian, X.-B. Qiang, H. Zhou, J. Shen, H. Lu, T.-R. Chang, Z. Qu, and S. Jia, Topological charge-entropy scaling in kagome Chern magnet $\mathrm{TbMn_6Sn_6}$ (2021), arXiv:2110.07563 [cond-mat.str-el].

[15] L. Gao, S. Shen, Q. Wang, W. Shi, Y. Zhao, C. Li, W. Cao, C. Pei, J.-Y. Ge, G. Li, J. Li, Y. Chen, S. Yan, and Y. Qi, Anomalous Hall effect in ferrimagnetic metal $R\mathrm{Mn_6Sn_6}$ (R = Tb, Dy, Ho) with clean Mn kagome lattice, Applied Physics Letters **119**, 092405 (2021).

[16] S. X. M. Riberolles, T. J. Slade, D. L. Abernathy, G. E. Granroth, B. Li, Y. Lee, P. C. Canfield, B. G. Ueland, L. Ke, and R. J. McQueeney, Competing magnetic energy scales in the topological flat-band ferrimagnet $\mathrm{TbMn_6Sn_6}$ (2021), accepted by PRX, arXiv:2110.14713 [cond-mat.str-el].

[17] C. Mielke III, W. Ma, V. Pomjakushin, O. Zaharko, X. Liu, J.-X. Yin, S. Tsirkin, T. Cochran, M. Medarde, V. Poree, *et al.*, Intriguing magnetism of the topological kagome magnet $\mathrm{TbMn_6Sn_6}$, arXiv preprint arXiv:2101.05763 (2021).

[18] D. C. Jones, S. Das, H. Bhandari, P. Siegfried, M. P. Ghimire, S. Tsirkin, I. I. Mazin, and N. J. Ghimire, Origin of spin reorientation and intrinsic anomalous Hall effect in the kagome ferrimagnet $\mathrm{TbMn_6Sn_6}$ (2022), arXiv:2203.17246.

[19] B. Malaman, G. Venturini, R. Welter, J. Sanchez, P. Vulliet, and E. Ressouche, Magnetic properties of $R\mathrm{Mn_6Sn_6}$ (R =Gd–Er) compounds from neutron diffraction and Mössbauer measurements, Journal of Magnetism and Magnetic Materials **202**, 519 (1999).

[20] D. Clatterbuck and K. Gschneidner, Magnetic properties of $R\mathrm{Mn_6Sn_6}$ (R =Tb, Ho, Er, Tm, Lu) single crystals, Journal of Magnetism and Magnetic Materials **207**, 78

(1999).
[21] S. Kimura, A. Matsuo, S. Yoshii, K. Kindo, L. Zhang, E. Brück, K. Buschow, F. de Boer, C. Lefèvre, and G. Venturini, High-field magnetization of $R\mathrm{Mn_6Sn_6}$ compounds with R = Gd, Tb, Dy and Ho, Journal of Alloys and Compounds **408-412**, 169 (2006), proceedings of Rare Earths'04 in Nara, Japan.
[22] S. Tabatabai Yazdi, N. Tajabor, M. Rezaee Roknabadi, M. Behdani, and F. Pourarian, Magnetoelastic properties of $\mathrm{ErMn_6Sn_6}$ intermetallic compound, Journal of Magnetism and Magnetic Materials **324**, 723 (2012).
[23] J. Jensen and A. R. Mackintosh, *Rare earth magnetism* (Clarendon Press, Oxford, 1991).
[24] R. Verhoef, P. Quang, J. Franse, and R. Radwański, The strength of the R-T exchange coupling in $R_2\mathrm{Fe_{14}B}$ compounds, Journal of Magnetism and Magnetic Materials **83**, 139 (1990).
[25] J. Liu, F. de Boer, P. de Châtel, R. Coehoorn, and K. Buschow, On the $4f$-$3d$ exchange interaction in intermetallic compounds, Journal of Magnetism and Magnetic Materials **132**, 159 (1994).
[26] N. Duc, T. Hien, D. Givord, J. Franse, and F. de Boer, Exchange interactions in rare earth-transition metal compounds, Journal of Magnetism and Magnetic Materials **124**, 305 (1993).
[27] R. J. Radwański, The Intersublattice Molecular Fields in the Rare Earth-Cobalt Intermetallics, physica status solidi (b) **137**, 487 (1986).
[28] E. Belorizky, M. A. Fremy, J. P. Gavigan, D. Givord, and H. S. Li, Evidence in rare-earth (R)-transition metal (M) intermetallics for a systematic dependence of R-M exchange interactions on the nature of the R atom, Journal of Applied Physics **61**, 3971 (1987).
[29] N. D. Mermin and H. Wagner, Absence of Ferromagnetism or Antiferromagnetism in One- or Two-Dimensional Isotropic Heisenberg Models, Phys. Rev. Lett. **17**, 1133 (1966).
[30] V. V. Mkhitaryan and L. Ke, Self-consistently renormalized spin-wave theory of layered ferromagnets on the honeycomb lattice, Phys. Rev. B **104**, 064435 (2021).
[31] H. Kirchmayr and C. Poldy, Magnetism in rare earth-3d intermetallics, Journal of Magnetism and Magnetic Materials **8**, 1 (1978).
[32] L. Ke, Intersublattice magnetocrystalline anisotropy using a realistic tight-binding method based on maximally localized Wannier functions, Phys. Rev. B **99**, 054418 (2019).
[33] B. Li, J.-Q. Yan, D. M. Pajerowski, E. Gordon, A.-M. Nedić, Y. Sizyuk, L. Ke, P. P. Orth, D. Vaknin, and R. J. McQueeney, Competing Magnetic Interactions in the Antiferromagnetic Topological Insulator $\mathrm{MnBi_2Te_4}$, Phys. Rev. Lett. **124**, 167204 (2020).
[34] E. Gordon, V. Mkhitaryan, H. Zhao, Y. Lee, and L. Ke, Magnetic interactions and spin excitations in van der Waals ferromagnet $\mathrm{VI_3}$, Journal of Physics D: Applied Physics (2021).
[35] N. J. Ghimire, R. L. Dally, L. Poudel, D. C. Jones, D. Michel, N. T. Magar, M. Bleuel, M. A. McGuire, J. S. Jiang, J. F. Mitchell, J. W. Lynn, and I. I. Mazin, Competing magnetic phases and fluctuation-driven scalar spin chirality in the kagome metal $\mathrm{YMn_6Sn_6}$, Science Advances **6**, eabe2680 (2020).
[36] H. Bethe, Termaufspaltung in kristallen, Annalen der Physik **395**, 133 (1929).
[37] C. J. Ballhausen, *Introduction to ligand field theory* (McGraw-Hill, New York, 1962).
[38] D. J. Newman and B. Ng, The superposition model of crystal fields, Reports on Progress in Physics **52**, 699 (1989).
[39] M. Hutchings, Point-Charge Calculations of Energy Levels of Magnetic Ions in Crystalline Electric Fields (Academic Press, 1964) pp. 227–273.
[40] R. Skomski and J. M. D. Coey, *Permanent magnetism* (Institute of Physics Publishing, Bristol, 1999).
[41] R. Skomski, *Simple Models of Magnetism*, Oxford Graduate Texts (University Press, Oxford, 2008).
[42] K. N. R. Taylor and M. I. Darby, *Physics of rare earth solids* (Chapman and Hall, London, 1972).
[43] A. G. Petukhov, I. I. Mazin, L. Chioncel, and A. I. Lichtenstein, Correlated metals and the LDA + u method, Phys. Rev. B **67**, 153106 (2003).
[44] F. D. M. Haldane, Model for a Quantum Hall Effect without Landau Levels: Condensed-Matter Realization of the "Parity Anomaly", Phys. Rev. Lett. **61**, 2015 (1988).
[45] G. hua Guo and H. bei Zhang, Magnetocrystalline anisotropy and spin reorientation transition of $\mathrm{HoMn_6Sn_6}$ compound, Journal of Alloys and Compounds **429**, 46 (2007).
[46] L. Ke and M. van Schilfgaarde, Band-filling effect on magnetic anisotropy using a Green's function method, Phys. Rev. B **92**, 014423 (2015).
[47] L. Ke, D. A. Kukusta, and D. D. Johnson, Origin of magnetic anisotropy in doped $\mathrm{Ce_2Co_{17}}$ alloys, Phys. Rev. B **94**, 144429 (2016).
[48] L. Ke and D. D. Johnson, Intrinsic magnetic properties in $R(\mathrm{Fe}_{1-x}\mathrm{Co}_x)_{11}\mathrm{Ti}Z$ (R=Y and Ce; Z=H, C, and N), Phys. Rev. B **94**, 024423 (2016).
[49] P. Blaha, K. Schwarz, G. K. H. Madsen, D. Kvasnicka, J. Luitz, R. Laskowski, F. Tran, and L. D. Marks, *WIEN2k: An Augmented Plane Wave plus Local Orbitals Program for Calculating Crystal Properties* (Vienna University of Technology, Austria, 2018).
[50] J. P. Perdew, K. Burke, and M. Ernzerhof, Generalized Gradient Approximation Made Simple, Phys. Rev. Lett. **77**, 3865 (1996).
[51] N. Marzari and D. Vanderbilt, Maximally localized generalized Wannier functions for composite energy bands, Phys. Rev. B **56**, 12847 (1997).
[52] A. A. Mostofi, J. R. Yates, G. Pizzi, Y.-S. Lee, I. Souza, D. Vanderbilt, and N. Marzari, An updated version of wannier90: A tool for obtaining maximally-localised Wannier functions, Computer Physics Communications **185**, 2309 (2014).
[53] I. Souza, N. Marzari, and D. Vanderbilt, Maximally localized Wannier functions for entangled energy bands, Phys. Rev. B **65**, 035109 (2001).
[54] N. Marzari, A. A. Mostofi, J. R. Yates, I. Souza, and D. Vanderbilt, Maximally localized Wannier functions: Theory and applications, Rev. Mod. Phys. **84**, 1419 (2012).
[55] M. Li, Q. Wang, G. Wang, Z. Yuan, W. Song, R. Lou, Z. Liu, Y. Huang, Z. Liu, H. Lei, Z. Yin, and S. Wang, Dirac cone, flat band and saddle point in kagome magnet $\mathrm{YMn_6Sn_6}$, Nature Communications **12**, 3129 (2021).
[56] Y. Lee, T. Kotani, and L. Ke, Role of nonlocality in exchange correlation for magnetic two-dimensional van der Waals materials, Phys. Rev. B **101**, 241409 (2020).

[57] L. Ke and M. I. Katsnelson, Electron correlation effects on exchange interactions and spin excitations in 2D van der Waals materials, npj Computational Materials **7**, 1 (2021).

[58] A. L. Kutepov, Electronic structure of van der Waals ferromagnet CrI_3 from self-consistent vertex corrected *GW* approaches, Phys. Rev. Materials **5**, 083805 (2021).

Supplementary information for:

Ab initio studies of electronic structures and magnetic properties in $R\mathrm{Mn_6Sn_6}$ ($R =$ Gd, Tb, Dy, Ho, and Er)

Supplementary Figures Supplementary Tables Supplementary Theories and Methods Supplementary Discussions

I Supplementary Figures

II Supplementary Tables

III Supplementary Theories and Methods

IV Supplementary Discussions

I. SUPPLEMENTARY FIGURES

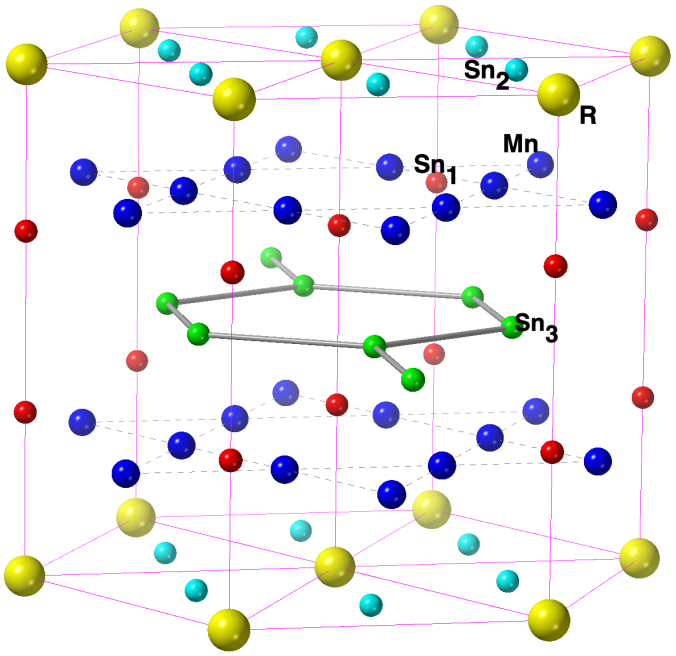

FIG. S1. Crystal structure of RMn$_6$Sn$_6$. The primitive unit cell is tripled to better illustrate the Mn Kagome lattice. RMn$_6$Sn$_6$ with heavy R elements crystallizes in the hexagonal HfFe$_6$Ge$_6$-type (or equivalently MgFe$_6$Ge$_6$-type; $P6/mmm$, space group no. 191) structure. The primitive cell contains one formula unit (f.u.). R atoms occupy the $1a$ (D_{6h}, or $6/mmm$) site, forming a triangular lattice in the basal plane. Sn$_2$ atoms occupy the $2d$ ($\bar{6}m2$) site located at the center of the R triangles, forming a honeycomb lattice; vice versa, R atoms are located in the centers of Sn$_2$ hexagons. Mn atoms occupy the $6i(2mm)$ site, forming two layers of the Kagome lattice in the unit cell. Sn$_1$ atoms occupy the $2e(6mm)$ site, forming two layers of triangular lattice, adjacent to the Mn layers. Sn$_1$ atoms form -Sn$_1$-Sn$_1$-R- chains along the c axis with R atoms and are pushed slightly off the Mn Kagome plane by R atoms. Sn$_3$ atoms occupy the $2c(\bar{6}m2)$ site, similar to Sn$_2$, forming a honeycomb lattice by itself and sandwiched between two Sn$_1$ layers. These layers are stacked in the order of [R-Sn$_2$]-Mn-Sn$_1$-Sn$_3$-Sn$_1$-Mn-[R-Sn$_2$] along the c axis.

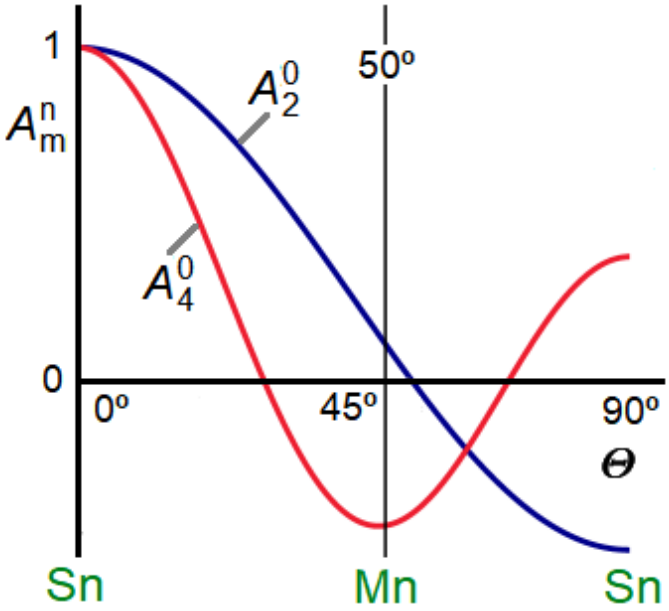

FIG. S2. Atomic coordination origin of large high-order crystal-field parameters and anisotropy contributions in RMn$_6$Sn$_6$. The relation between the crystal-field parameters and the atomic structure is given by the intrinsic crystal-field parameters A'_2 and A'_4. Simplifying somewhat, these parameters describe the interaction strength with the Mn and Sn ligands as far as the leading anisotropy contribution by the rare-earth atoms is concerned. For example, $A^0_2 = \frac{1}{2}A'_2(3\cos 2\Theta - 1)$, where Θ is the coordination angle, means that axial coordination ($\Theta = 0°$) and in-plane coordination ($\Theta = 90°$) yield opposite anisotropy contributions. The corresponding 4th-order expression is $A^0_4 = 1/8A'_4(35\cos 4\Theta - 30\cos 2\Theta + 3)$. The presence of energy minimum or maximum near 45° reflects the competition between K_1 and K_2, that is, between A^0_2 and A^0_4. The figure assumes normalized parameters $A'_2 = A'_4 = 1$, but in reality, $A'_2 \gg A'_4$. To make A'_4 competitive, it is necessary to have Mn and Sn coordinations that minimize A^0_2 but maximize A^0_4. Indeed, A^0_2 is very small, because the coordination of the Mn (about 50°) is close to the point where $A^0_2 = 0$, whereas the contributions of the axially (0°) and in-plane (90°) coordinated Sn atoms largely cancel each other. By contrast, the magnitudes of the A^0_4 contributions of both Mn and Sn are maximized. We also estimated these phenomenological CFP using CF levels of GdMn$_6$Sn$_6$ that calculated in DFT and obtained $A^0_2\langle r^2\rangle = 5.75$ meV and $A^0_4\langle r^4\rangle = -9.45$ meV.

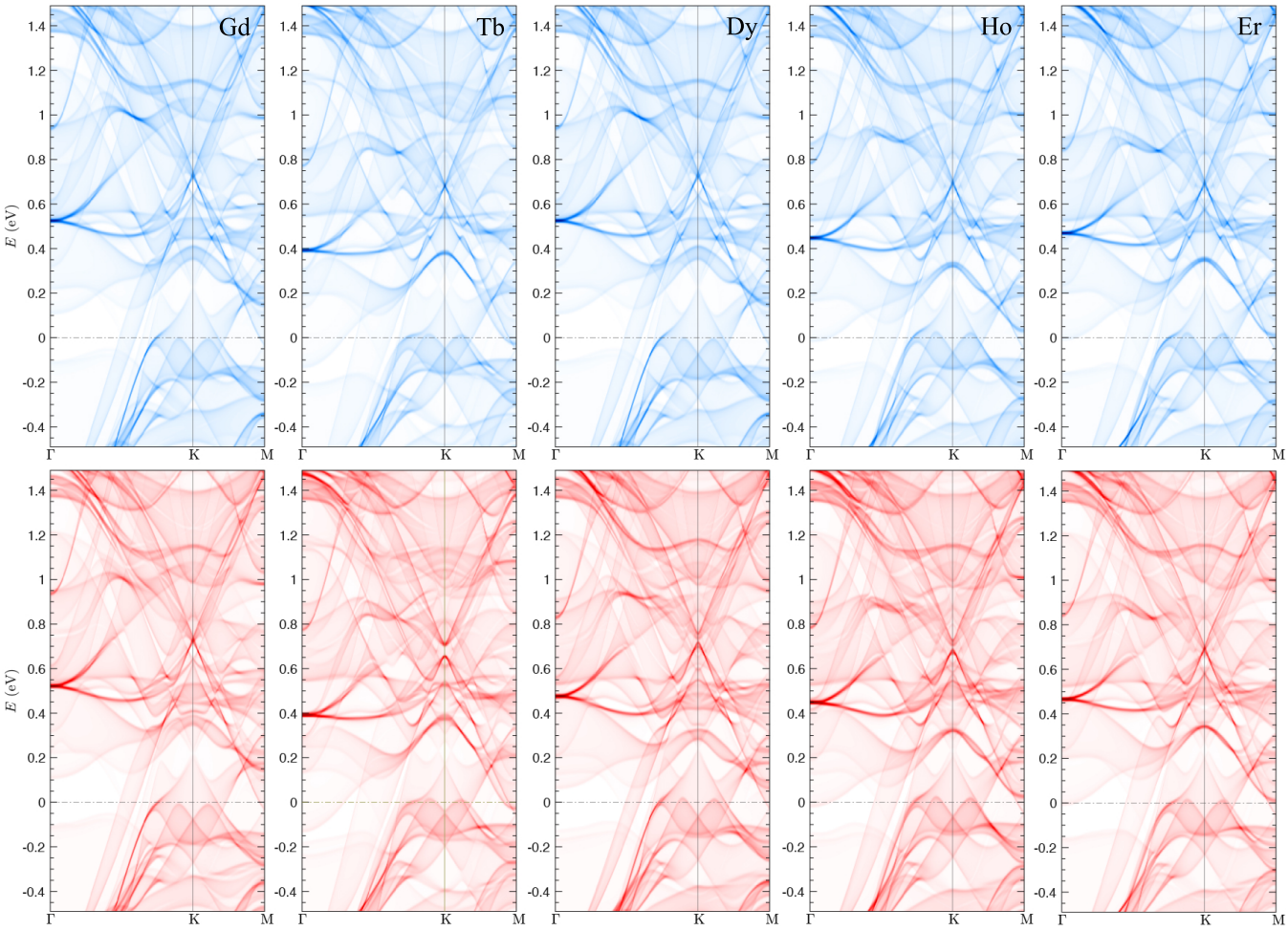

FIG. S3. The band structures projected on surface BZ near the Fermi level in RMn$_6$Sn$_6$ with R = Gd, Tb, Dy, Ho, and Er, calculated without (in blue) and with (in red) SOC. R-4f electrons are treated in the open-core approach in DFT and R-4f electrons are configured to satisfy Hund's first rule. A Gaussian smearing of 5 meV is used for the k_z-integration of spectral functions. For the SOC cases, the spin quantization axis directions are set to be along the easy direction of each compound. More specifically, $\theta_{\mathrm{Gd}} = 90°$, $\theta_{\mathrm{Tb}} = 0°$, $\theta_{\mathrm{Dy}} = 45°$, $\theta_{\mathrm{Ho}} = 49°$, and $\theta_{\mathrm{Er}} = 90°$. Overall, the band structures near E_{F}, consisting of non-4f states, share great similarities in all compounds. Multiple DCs occur at K, below and above E_{F}. All of them show an well expressed DC at ~ 0.7 eV, which can be gapped by SOC, as we discussed above for R = Tb and Ho. The difference between these band structures can be attributed to the variations of lattice parameters and the strength of R-5d moment and exchange splittings enhanced by various sizes of R-4f spin.

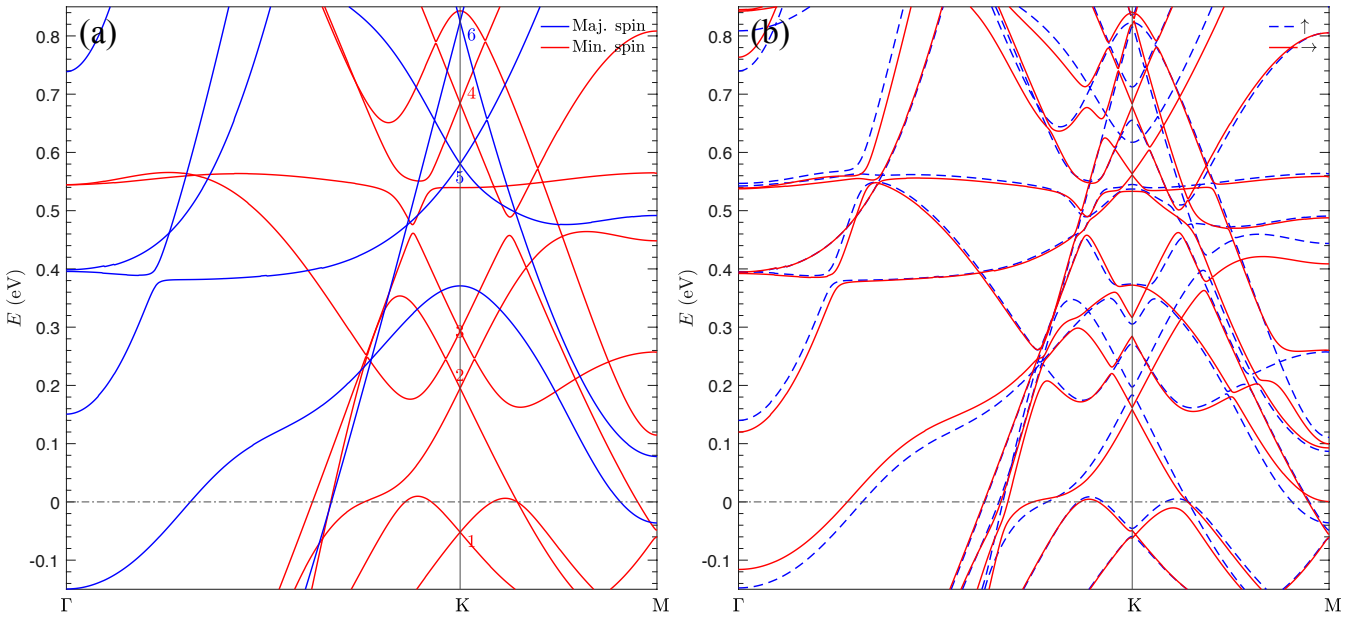

FIG. S4. Band structure near E_F in $TbMn_6Sn_6$ calculated (a) without SOC and (b) with SOC. In panel (a), the majority-spin and minority-spin, referred to Mn site, are in blue and red, respectively. In panel (b), the band structures are calculated with the spin-quantization axis along the out-of-plane (blue dashed line) and in-plane (red solid line) directions. Both magnetic sublattices are ordered. The gap sizes depend on spin orientations.

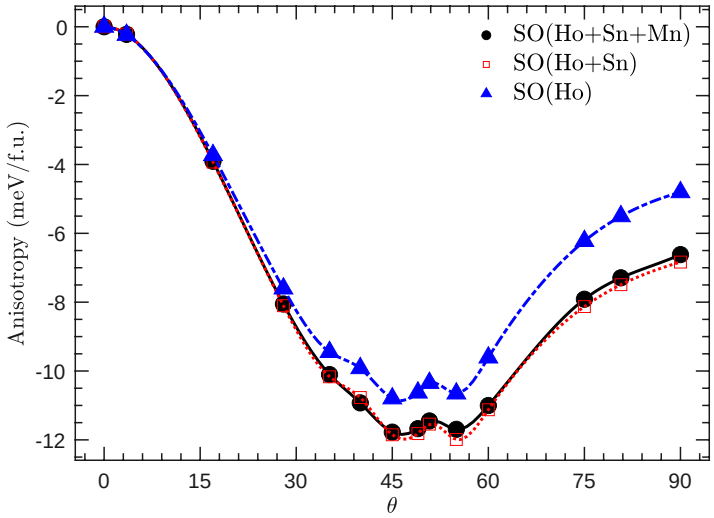

FIG. S5. Variation of magnetic energy (in meV/f.u.) as a function of spin-quantization-axis rotation in $HoMn_6Sn_6$, calculated with and without turning on SOC on Sn and Mn sites. θ is the angle between the spin direction and the out-of-plane direction. The black circles denote the regular full-SOC calculations with SOC turning on all sublattices. The red squares are calculated with SOC on Ho and Sn sublattices only, barely deviating from the full-SOC calculations (black circles). The blue triangles denote the calculations with Ho SOC only, showing the Ho sublattice, by itself, prefers the $\sim\theta = 49°$ orientation. Turning off Sn SOC also increases $E(\theta = 90°)$ by $\sim$2 meV/f u , which is the value of the above discussed easy-plane Mn anisotropy. Thus, Mn MA originates from the interplay between the Mn-3d spin polarization and the large Sn-4p SOC.

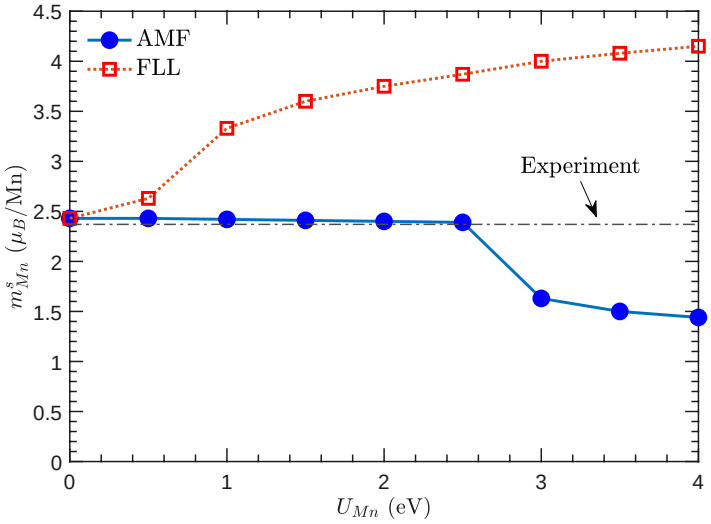

FIG. S6. The dependence of on-site Mn spin magnetic moment m^s_{Mn} in $TbMn_6Sn_6$ on U_{Mn} calculated within DFT+U using the around-mean-field (AMF) and the fully-localized-limit (FLL) double-counting schemes. Hubbard U is applied on Mn-3d orbitals. The calculations are performed in a full-potential LMTO method without SOC, confirming the same trends we obtained in WIEN2K. The Mn spin moment m^s_{Mn} calculated in the AMF scheme agrees well with the experiment with $U = 0$–$2.5\,\mathrm{eV}$, while the FLL scheme tends to overestimate m^s_{Mn}.

II. SUPPLEMENTARY TABLES

TABLE S1. The coefficients (multiply by 1024 for readability) of $e_0, e_{\pm1}, e_{\pm2}, e_{-3}$ in anisotropy parameters C_i^m and $C_i^{n_\downarrow}$, with $i = 0$, 2, 4, 6. Note that $C_i^{f^1} = C_i^{\pm3}$. We also have $C_i^{f^4} = -C_i^{f^3}$, $C_i^{f^5} = -C_i^{f^2}$, $C_i^{f^6} = -C_i^{f^1}$, and $C_i^{f^7} = 0$.

	$m=\pm3$				$m=\pm2$				$m=\pm1$				$m=0$			f^2				f^3		
C	e_0	e_1	e_2	e_{-3}	e_0	e_1	e_2	e_{-3}	e_0	e_1	e_2	e_{-3}	e_0	e_1	e_2	e_0	e_1	e_2	e_{-3}	e_0	e_1	e_2
C_0	100	210	252	-276	120	260	392	96	156	398	260	180	272	312	240	220	470	-380	-180	376	-156	-120
C_2	-150	-255	-90	240	-60	-70	220		54	271	-70	-240	312	108	-120	-210	-325	130	240	-156	-54	60
C_4	60	30	-156	36	-120	-100	376	-96	-60	130	-100	60	240	-120	-240	-60	-70	220	-60	-120	60	120
C_6	-10	15	-6		60	-90	36		-150	225	-90		200	-300	120	50	-75	30		-100	150	-60

TABLE S2. $HoMn_6Sn_6$ band characters of six Dirac crossings near E_F at BZ corners K, as indicated in Fig. 8(a), resolved into sublattices (per sublattice) and Mn-3d orbitals (per Mn atom). The majority and minority spin channels are referred to Mn sites.

	Minority Spin				Majority Spin	
Index	1	2	3	4	5	6
$E - E_F$ (eV)	-0.065	0.243	0.260	0.705	0.585	0.812
Ho	0.012	0.034	0.059	0.003	0.053	0.102
Mn	0.831	0.697	0.690	0.856	0.554	0.477
Sn	0.026	0.080	0.040	0.021	0.190	0.138
Interstitial	0.131	0.189	0.211	0.121	0.203	0.283
d_{xy}	0.009	0.026	0.001	0.091	0.075	0.000
d_{yz}	0.000	0.010	0.016	0.000	0.000	0.052
d_{z^2}	0.110	0.001	0.003	0.021	0.000	0.000
d_{xz}	0.002	0.000	0.093	0.000	0.000	0.011
$d_{x^2-y^2}$	0.015	0.076	0.000	0.025	0.012	0.000

TABLE S3. $TbMn_6Sn_6$ band characters of six Dirac crossings near E_F at BZ corners K, as indicated in Fig. S4, resolved into sublattices (per sublattice) and Mn-3d orbitals (per Mn atom). Majority and minority spin chanels are refered to Mn sites.

	Minority Spin				Majority Spin	
Index	1	2	3	4	5	6
$E - E_F$ (eV)	-0.052	0.195	0.293	0.684	0.580	0.826
Tb	0.018	0.038	0.054	0.002	0.057	0.062
Mn	0.817	0.690	0.699	0.854	0.546	0.492
Sn	0.025	0.080	0.038	0.022	0.189	0.144
Interstitial	0.139	0.191	0.209	0.122	0.210	0.301
d_{xy}	0.009	0.025	0.001	0.092	0.073	0.000
d_{yz}	0.002	0.011	0.015	0.000	0.000	0.054
d_{z^2}	0.105	0.001	0.007	0.021	0.000	0.002
d_{xz}	0.004	0.002	0.090	0.000	0.000	0.011
$d_{x^2-y^2}$	0.015	0.076	0.002	0.024	0.012	0.000

III. SUPPLEMENTARY THEORIES AND METHODS

A. Crystal structure

Figure S1 shows the crystal structure, where the primitive cell is tripled to illustrate the Mn kagome lattice better. Lattice parameters of RMn$_6$Sn$_6$ change with R. Experiments found that TbMn$_6$Sn$_6$ has the largest volume, while GdMn$_6$Sn$_6$ has the smallest volume. For all RMn$_6$Sn$_6$ except TbMn$_6$Sn$_6$, the distance between neighboring Mn layers are slightly larger across the Sn$_1$ and Sn$_3$ layers than the one across the [R-Sn$_2$] layer. These two inter-Mn-plane distances are accidentally the same in TbMn$_6$Sn$_6$. The crystal structure can also be described as a filled derivative of the CoSn $B35$-type structure and closely related to the CaCu$_5$-type [47] and ThMn$_{12}$-type [48] structures [7]. It is worth noting that the RMn$_6$Sn$_6$ structure shares great similarity to that of the famous SmCo$_5$ magnet [7, 47], but with two different kinds of ligand atoms and with the nearest Sn$_1$ neigbor along the axial direction, resulting in a drastically different R anisotropy than in RCo$_5$. RMn$_6$Sn$_6$ with light R elements have a different crystal structure.

B. *Ab initio* methods for calculating electronic structures

DFT calculations are performed using a full-potential linear augmented plane wave (FP-LAPW) method, as implemented in WIEN2K [49]. The generalized gradient approximation of Perdew, Burke, and Ernzerhof [50] is used for the correlation and exchange potentials. To generate the self-consistent potential and charge, we employed $R_{\rm MT} \cdot K_{\rm max} = 8.0$ with muffin-tin (MT) radii $R_{\rm MT} = 2.7$, 2.4, and 2.5 a.u., for R, Mn, and Sn, respectively. The calculations are performed with 264 k-points in the irreducible Brillouin zone (IBZ). They are iterated until charge differences between consecutive iterations are smaller than 10^{-3} e and the total energy differences lower than 0.01 mRy. Low-temperature experimental lattice parameters [7] are adopted in all bulk calculations, and SOC is included using a second variational method.

The strongly correlated R-4f electrons are treated in both the DFT+U method using the fully-localized-limit (FLL) double-counting scheme and the so-called open-core approach. For DFT+U calculations, the initial orbital occupancy of 4f states are controlled to ensure that the self-consistent electron configurations satisfy Hund's rules and consistent with experiments. It is worth noting that DFT+U may not find the correct experimental R-4f configurations as the ground states. To properly describe magnetic properties, especially R-4f magnetocrystalline anisotropy, it is crucial to converge the DFT+U calculations to the solutions that are consistent with experiments. In the open-core approach, occupied 4f electrons are included as core states, which is a reasonable approximation when describing the band structures near the Fermi level with negligible 4f contributions. Moreover, we use the open-core approach to investigate the contributions of non-4f electron on MA. Besides the R-4f orbitals, we also explore the effects of Mn-3d electron correlation on band structure near $E_{\rm F}$ by applying Hubbard U on Mn-3d orbitals in DFT+U while treating R-4f in the open-core approach. Considering the more itinerant nature of Mn-3d states in metallic RMn$_6$Sn$_6$, we mainly use the around-mean-field (AMF) double-counting scheme, which is also found to describe better the Mn magnetic moment than the FLL scheme in RMn$_6$Sn$_6$.

The band structures near $E_{\rm F}$ are further analyzed using an in-house *ab initio* tight-binding (TB) framework [32]. Realistic TB Hamiltonians are constructed via the maximally localized Wannier functions (MLWFs) method [51] as implemented in WANNIER90 [52] through a post-processing procedure [51, 53, 54] using the output of the self-consistent DFT calculations. We construct the TB Hamiltonian using 118 MLWFs, which correspond to d-type orbitals for R and Mn, and s- and p-type orbitals for Sn in the unit cell. Note that the 59 orbitals are doubled to account for SOC, which mixes the two spin channels. A real-space Hamiltonian $H(\mathbf{R})$ with dimensions 118×118 is constructed to accurately represent the band structures in the energy window of interest.

C. Magnetocrystalline anisotropy in Rare-earth compounds

In general, the Mn spins in RMn$_6$Sn$_6$ prefer the in-plane direction while the easy-axis of the R atoms varies with the type of R atom and may be incompatible with Mn. For the R sublattice, due to the strong SOC, electronic configurations of 4f shell obey the third Hund's rules [41]. The magnetic moment of 4f electrons is strongly coupled with the anisotropic-shaped charge cloud, which is determined by superposing the occupied spherical harmonics of $|l = 3, m\rangle$ with various m channels. The charge cloud orients accordingly with respect to the CF of surrounding lattices to minimize the Coulomb energy, giving the strong 4f-electron MA.

To identify the easy direction and MA energy (MAE) of RMn$_6$Sn$_6$, we calculate the total energies of their collinear (ferrimagnetic) states in DFT+U as a function of magnetic quantization direction. The calculations are controlled to converge to the solutions consistent with experiments, in which the R-4f electron configurations satisfy Hund's rules.

Furthermore, we also use various approaches to resolve the MAE contribution into different sublattices. For example, to explore the non-$4f$ contribution to MAE dominated at high temperatures, we include R-$4f$ in the open core and constrain their moments to be zero to mimic a disordered $4f$ moment. On the other hand, we also investigate the R-only contribution by turning off the SOC on Mn and Sn sites in MAE calculations.

D. Spin-orientation-dependence of electronic structure

The magnetic structures, more specifically, the spin orientations of R and Mn atoms, are known to evolve with R and temperature. The moment directions and sizes directly impact the topology of the electronic band structure, and we calculate how band structures near E_{F}, especially the position of DCs and SOC-induced gap openings, depend on spin orientations.

As we show later, the Dirac bands are mainly characterized by non-$4f$, mostly the Mn-$3d$ orbitals. The sizes of SOC-induced gaps and their dependence on the spin-quantization-axis direction can be understood by including the SOC term in the single-particle Hamiltonian within a perturbation theory [46]. For an arbitrary spin-quantization direction $\hat{\mathbf{n}} = (\theta, \varphi)$, the SOC Hamiltonian can be written as

$$H_{\mathrm{so}}(\hat{\mathbf{n}}) = \frac{\xi}{2} U(\theta,\varphi)(\mathbf{L}\cdot\mathbf{S})U^{\dagger}(\theta,\varphi)\,. \tag{S1}$$

Here, ξ is the SOC constant depending on orbital l and site i, and $U(\theta,\varphi)$ is the unitary transformation Wigner matrix (See details in Appendix A in Ref. [32]). Thus, we obtain

$$H_{\mathrm{so}}\,(\theta,\varphi) = \frac{\xi}{2}\begin{pmatrix} A & B \\ B^{\dagger} & -A \end{pmatrix}, \tag{S2}$$

where the spin-parallel component A and the spin-flip component B are written as

$$A(\theta,\varphi) = \cos(\theta)L_z + \frac{1}{2}\sin(\theta)\left(e^{i\varphi}L_- + e^{-i\varphi}L_+\right) \tag{S3}$$

$$B(\theta,\varphi) = -\sin(\theta)L_z + \frac{1}{2}\Big(\left(\cos(\theta)+1\right)e^{i\varphi}L_- + \left(\cos(\theta)-1\right)e^{-i\varphi}L_+\Big). \tag{S4}$$

E. MAE analytical modeling using calculated CF energies

The full Hamiltonian matrix of atom R can be written as

$$H_{mm'} = H_{\mathrm{SO}} + H_{\mathrm{CF}} = \left\langle \tilde{Y}_{lm}|\xi\mathbf{L}\cdot\mathbf{S}|\tilde{Y}_{lm'}\right\rangle + \left\langle \tilde{Y}_{lm}|H_{\mathrm{CF}}|\tilde{Y}_{lm'}\right\rangle, \tag{S5}$$

The anisotropy energy of $4f$ states, the angular dependence of CF energy, can be expressed in terms of CF levels $\epsilon = [e_{-3}\, e_{-2}\, e_{-1}\, e_0\, e_1\, e_2\, e_3]^{\intercal}$. In the absence of SOC, orbitals are fully quenched and the eigenstates are characterized by the *real* spherical harmonics $\mathcal{Y}^l_m$. In the limit of $\xi \gg d$, instead, the eigenstates are characterized by rotated *complex* spherical harmonics $\tilde{Y}_m(\theta)$, where $\tilde{Y}_m(\theta=0) = Y_m$. Expressing $\langle\tilde{Y}_m|H_{\mathrm{CF}}|\tilde{Y}_{m'}\rangle$ in terms of $\langle\mathcal{Y}_m|H_{\mathrm{CF}}|\mathcal{Y}_{m'}\rangle$ is achieved by a Wigner rotation followed by an unitary transformation $\tilde{Y} \to Y \to \mathcal{Y}$.

$$\tilde{Y}^l_{m_2}(\theta) = \sum_{m_1} Y^l_{m_1} D^l_{m_1 m_2}(\theta) \tag{S6}$$

$$Y^l_{m_2} = \sum_{m_1} \mathcal{Y}^l_{m_1} U_{m_1 m_2} \tag{S7}$$

Note that, the corresponding Wigner rotation matrix $D^l_{mm'}(\theta) = D^l_{mm'}(\alpha=0,\beta=\theta,\gamma=0)$ is a real matrix and $D^{\dagger} = D^{\intercal}$. In DFT calculation, we rotate the spin axis from z axis to y axis, which corresponds to rotations that characterized by the Euler angles $(\alpha=0,\beta=\theta,\gamma=0)$. For the f block, the unitary transformation matrix $\mathbf{U}$ is

$$\mathbf{U} = \mathbf{U}_{\mathbb{R}\leftarrow\mathbb{C}} = \frac{1}{\sqrt{2}}\begin{pmatrix} -i & 0 & 0 & 0 & 0 & 0 & -i \\ 0 & -i & 0 & 0 & 0 & i & 0 \\ 0 & 0 & -i & 0 & -i & 0 & 0 \\ 0 & 0 & 0 & \sqrt{2} & 0 & 0 & 0 \\ 0 & 0 & 1 & 0 & -1 & 0 & 0 \\ 0 & 1 & 0 & 0 & 0 & 1 & 0 \\ 1 & 0 & 0 & 0 & 0 & 0 & -1 \end{pmatrix} \tag{S8}$$

For simplicity, in the following, we absorb (θ) and $l=3$ in $\tilde{Y}^l_m(\theta)$ and $D^l_{mm'}(\theta)$. The matrix element of $H_{\rm CF}$ in the basis of $|\tilde{Y}_m\rangle$ becomes:

$$\begin{aligned}\langle\tilde{Y}_m|H_{\rm CF}|\tilde{Y}_{m'}\rangle &= \sum_{m_1m_2m_3m_4}\langle\tilde{Y}_m|Y_{m_1}\rangle\langle Y_{m_1}|\mathcal{Y}_{m_2}\rangle\langle\mathcal{Y}_{m_2}|V|\mathcal{Y}_{m_3}\rangle\langle\mathcal{Y}_{m_3}|Y_{m_4}\rangle\langle Y_{m_4}|\tilde{Y}_{m'}\rangle \\ &= \sum_{m_1m_2m_3m_4} D^\dagger_{m,m_1}U^\dagger_{m,m_2}V_{m_2,m_3}U_{m_3,m_4}D_{m_4m'} \\ &= (\mathbf{D}^\dagger\mathbf{U}^\dagger\mathbf{E}\mathbf{U}\mathbf{D})_{mm'}\end{aligned} \tag{S9}$$

Here, $\mathbf{E}$ is the diagonal matrix with element of $\langle\mathcal{Y}_{m_1}|V|\mathcal{Y}_{m_2}\rangle = e_{m_1}\delta_{m_1,m_2}$. In RMn$_6Sn_6$, we have $e_0 = E(a_{2u})$, $e_{\pm1} = E(e_{1u})$, $e_{\pm2} = E(e_{2u})$, $e_{-3} = E(b_{1u})$ and $e_3 = E(b_{2u})$. Note that, matrix $(\mathbf{U}^\dagger\mathbf{E}\mathbf{U})$ have diagonal elements $(\mathbf{U}^\dagger\mathbf{E}\mathbf{U})_{\pm3,\pm3} = (e_{-3}+e_3)/2$ and off-diagonal elements $(\mathbf{U}^\dagger\mathbf{E}\mathbf{U})_{\pm3,\mp3} = (e_{-3}-e_3)/2$, which differs from the diagonal matrix $\mathbf{E}$. In the following, we set e_3 as the energy reference zero.

$$K_m = \langle\tilde{Y}_m|H_{\rm CF}|\tilde{Y}_m\rangle = D_{-3,m}D_{3,m}e_{-3} + \sum_{m'}(D_{m'm})^2e_{m'} \tag{S10}$$

$$K_n = \sum_{m=3}^{4-n} K_m \tag{S11}$$

For Tb case,

$$K_{\rm Tb} = K(f^1) = K_{m=3} = \langle\tilde{Y}_3|H_{\rm CF}|\tilde{Y}_3\rangle = \sum_m (D_{m3})^2e_m + D_{3,-3}D_{33}e_{-3} \tag{S12}$$

The m-orbital contribution to anisotropy, $K_m(\theta)$, can be written as

$$K_m(\theta) = C_0^m + C_2^m\cos(2\theta) + C_4^m\cos(4\theta) + C_6^m\cos(6\theta) \tag{S13}$$

Here, the parameters C_i^m are linear combinations of e_j, and the corresponding coefficients are tabulated in Table S1. For more than one $4f$ electrons, we have

$$K_{f^{n_\downarrow}} = \sum_{m=-3}^{n-4} K_m \tag{S14}$$

As expected, in this simple model, we have

$$\begin{aligned}K_m(\theta) &= K_{-m}(\theta) \\ \sum_{m=-3}^{3} K_m(\theta) &= 0\end{aligned} \tag{S15}$$

From these equations, we also have $K(f^n) = -K(f^{7-n})$.

For f^1,

$$\begin{aligned}K_{\rm Tb} = \frac{1}{1024}\big(&(100e_0+210e_1+252e_2-276e_{-3}) \\ &+(-150e_0-255e_1-90e_2+240e_{-3})\cos2\theta \\ &+(60e_0+30e_1-156e_2+36e_{-3})\cos4\theta \\ &+(-10e_0+15e_1-6e_2)\cos6\theta\big),\end{aligned} \tag{S16}$$

for f^2

$$\begin{aligned}K_{\rm Dy} = \frac{1}{1024}\big(&(220e_0+470e_1-380e_2-180e_{-3}) \\ &+(-210e_0-325e_1+130e_2+240e_{-3})\cos2\theta \\ &+(-60e_0-70e_1+220e_2-60e_{-3})\cos4\theta \\ &+(50e_0-75e_1+30e_2)\cos6\theta\big),\end{aligned} \tag{S17}$$

for f^3

$$\begin{aligned} K_{\mathrm{Ho}} = \frac{1}{1024}\big((376e_0 - 156e_1 - 120e_2) \\ + (-156e_0 - 54e_1 + 60e_2)\cos 2\theta \\ + (-120e_0 + 60e_1 + 120e_2)\cos 4\theta \\ + (-100e_0 + 150e_1 - 60e_2)\cos 6\theta\big), \end{aligned} \tag{S18}$$

We use the CF energy levels calculated in Gd, $e_0 = 33.44, e_{\pm 1} = 76.84, e_{\pm 2} = 90.2, e_{-3} = 67.42$ (meV).

IV. SUPPLEMENTARY DISCUSSIONS

A. Orbital characters of Dirac crossings near E_F

To understand the k_z dependence of surface bands and how the Dirac crossings and SOC-induced gaps evolve with spin orientation, we analyze the corresponding orbital characters at these band crossings. Figure 8(a) shows the band structure in $HoMn_6Sn_6$ calculated without SOC along the high symmetry path Γ-K-M ($k_z = 0$). Six DCs, indexed as 1–6 in Fig. 8(a), occur within the energy window; four (DC1–DC4) in the minority Mn-spin channel, and two (DC5, DC6) in the majority Mn-spin channel. The band characters of these DCs are resolved into atoms and Mn-3d orbitals, as listed in Table S2.

Band characters are dominated by Mn-3d orbitals while showing hybridization with Ho and Sn sites. In comparison to other crossings, two DCs in the majority spin channel, DC5 and DC6, have more substantial amounts of contributions from Ho and Sn, especially the latter, resulting in a stronger k_z dependence, as shown in Fig. 7. In contrast, DC4 and DC1 in the minority spin channel, consisting of the least amount of Sn and Ho characters, show strong intensity in Fig. S3.

The size of the SOC-induced gap and its dependence on spin quantization direction can be understood by further resolving the band characters into Mn-3d orbitals. DC4 consists d_{xy} ($|m = -2\rangle$), d_{z^2} ($|m = 0\rangle$), and $d_{x^2-y^2}$ ($|m = 2\rangle$) characters. The SOC Hamiltonian, more specifically, the L_z operator, couples $|m = \pm 2\rangle$ states and effectively opens up a gap. On the other hand, DC1 consists of more $|m = 0\rangle$ states and less $|m = \pm 2\rangle$ states, resulting in a much smaller SOC-induced gap. DC5 contains Mn-$|\pm 2\rangle$ states and also a substantial amount of Sn-p states, which have a large SOC constant, giving a large gap, as shown in Fig. 8(b).

$TbMn_6Sn_6$ shows the similar orbital characters, as shown in Table S2 and Fig. S4.

B. Effects of Mn-3d electron correlation

As mentioned, the position of the quasi-2D Dirac crossing is far above E_F and unlikely to play a significant role in transport properties. On the other hand, it is unclear whether the plain DFT treatment of Mn sublattice in RMn_6Sn_6 is sufficient. Indeed, for example, a sizable Hubbard $U = 4$ eV had been applied on Mn-3d orbitals in DFT+DMFT to describe the measured band structure in YMn_6Sn_6 [55], while most other studies treated Mn within DFT [13]. Finally, it is worth noting that the DMFT technique is known to generate grossly inaccurate results in itinerant systems unless ligand orbitals (in this case, Sn) are taken into account; and in a system with 12 atoms per cell, it is computationally unfeasible.

As we discuss in the main text, a qualitative idea about how additional electron repulsion to Mn-3d orbitals affects the position of the corresponding bands and DCs can be gained from (arguably oversimplified) DFT+U calculations in FLL and AMF double-counting schemes, and we presented in the main text our arguments in favor of the latter. Indeed, within the FLL scheme, the Mn magnetic moment quickly increases to $\sim 3.3\ \mu_B$/Mn at $U = 1$ eV, overestimating the experimental value of 2.4 μ_B/Mn, thus overestimating the exchange splitting as well. Therefore, below we only present band structures calculated using the AMF scheme.

Figure 7(b) shows the band structures calculated with $U_{Mn} = 2.5$ eV and $J_{Mn} = 0.7$ eV, showing a SOC-gapped DC located at $\sim$0.2 eV above E_F. Interestingly, the gap size is even larger than the one obtained in DFT, and the flat band near the 0.55 eV obtained in DFT is also lowered to 0.1 eV in DFT+U. The on-site Mn moment decreases to 2.2 μ_B/Mn. Thus, additional correlation effects on Mn-3d orbitals can profoundly affect topological band structures near E_F in these systems and are worth further investigation.

However, in general, the choice of the correlated orbitals and the associated on-site U and J are not well-defined for metallic systems. Moreover, off-site nonlocal exchange correlations can also play important roles [56, 57]. Thus, the comparison with ARPES results may be useful to determine the best U and J parameters (note that we expect correlation effects on Mn to be rather insensitive to the rare earth, so antiferromagnetic members of the family can be used as well). On the theoretical side, parameter-free method investigation of electron correlation effects [56–58] on electronic structures and magnetic properties could also be useful.